



universität
wien

MASTERARBEIT

Titel der Masterarbeit

„High optical and mechanical quality factor optomechanical devices“

Verfasserin

Karoline Siquans, BSc

angestrebter akademischer Grad

Master of Science (MSc)

Wien, 2014

Studienkennzahl lt. Studienblatt:

A 066876

Studienrichtung lt. Studienblatt:

Masterstudium Physik

Betreuerin / Betreuer:

Univ.-Prof. Dr. Markus Aspelmeyer

Acknowledgements

First, I would like to thank Markus Aspelmeyer for giving me the opportunity to work in his excellent research group at the University of Vienna. For me it meant the introduction into the "real" scientific world.

Then, I want to thank the people from the mirror team I worked in. Special thanks to Witlef Wiczorek who was a helpful advisor during the experimental phase of my thesis and also during the writing. Jason Hölscher-Obermaier took great care of me in the first month that I spent in the group, Ralf Riedinger supported me in many ways, and Claus Gärtner was a cheerful co-worker.

Thanks to Simon Gröblacher and Richard Norte, who fabricated the photonic crystal membranes at the California Institute of Technology, to Garrett Cole, who is fabricating the pillar structure devices and a great support in materials physics issues, to Sungkun Hong, who did the cleaning of the photonic crystal membranes, and to Jonas Schmöle, who was a funny and reliable colleague in setting up the fiber interferometer.

In general, I enjoyed the atmosphere in the whole group. Florian, Uros, David, Simon, Julian, Sebastian, Rainer, Nikolai, Philipp, Sahar, Alex, Tom - thank you for physics and other discussions.

I wish to explicitly thank my best friend Katharina Wittmann for always listening to me, giving advice, and cheering me up.

Finally, I want to mention my family, who are supporting me in all my plans and are there for me whenever I need them.

*Karoline Siquans
Vienna, December 2013*

Abstract

In optomechanical systems, the optical and mechanical properties of the mechanical resonator are of great importance. There do already exist various types of resonators of different shapes and materials (see e.g. ref. [1], [8], [43], [44]), but there is still the need for improvement.

In this thesis, the optical and mechanical properties of three mechanical devices are investigated. First, structures with an additional silicon pillar between the mechanical resonator and the mirror pad, which should entail better decoupling of the mechanics from the environment, are introduced. Then, a completely new generation of photonic crystal membranes is explored. They are designed such that a laser beam of a certain wavelength hitting them perpendicularly is reflected with a reflectivity approaching 1. This, in combination with mechanical quality factors around 10^6 , makes these devices promising new optomechanical structures. Finally, the mechanical quality factors for commercial stoichiometric silicon nitride membranes are measured for various holders and clamping methods at room temperature and cryogenic temperatures. The results of $Q > 10^6$ for certain modes with clamping that touches the membrane as little as possible, and the fact that at low temperatures there is an enhancement of Q of almost a factor of 5, are in good agreement with previous results from other groups.

Zusammenfassung

In optomechanischen Systemen sind die optischen und mechanischen Eigenschaften der mechanischen Resonatoren von großer Bedeutung. Bereits jetzt gibt es viele verschiedene Arten von Resonatoren unterschiedlicher Formen und Materialien (Ref. [1], [8], [43], [44]). Dennoch ist eine weitere Verbesserung dieser Strukturen notwendig.

In dieser Arbeit werden die optischen und mechanischen Eigenschaften von drei Oszillatoren untersucht. Zuerst werden Strukturen vorgestellt, die eine zusätzliche Silizium-Säule zwischen dem Spiegelpad und dem mechanischen Resonator besitzen, wodurch eine bessere Entkopplung der Mechanik von der Umgebung erzielt werden soll. Weiters wird eine völlig neue Generation von photonischen Kristall-Membranen erforscht. Sie sind so gebaut, dass ein senkrecht auftreffender Laserstrahl einer bestimmten Wellenlänge mit einer Reflektivität nahe 1 reflektiert wird. Die Kombination aus hoher Reflektivität und guten mechanischen Gütefaktoren Q von circa 10^6 macht diese Membranen zu vielversprechenden neuen optomechanischen Strukturen. Zuletzt werden die mechanischen Gütefaktoren von kommerziellen Siliziumnitrid-Membranen für verschiedene Halter und Klemmmethoden bei Raum- und Tieftemperatur untersucht. Die Resultate von $Q > 10^6$ für bestimmte Moden mit Befestigungen, die die Membran so wenig wie möglich berühren, stimmen ebenso mit den Ergebnissen von anderen Gruppen überein, wie die Tatsache, dass der Gütefaktor bei kryogenen Temperaturen fast um einen Faktor von

5 erhöht ist.

Contents

1	Introduction	1
2	Theory	3
2.1	Optomechanical Systems	3
2.1.1	Basic principle	3
2.1.2	Basic mathematical description of the system	4
2.2	Optical and Mechanical Dissipation	6
2.2.1	Optical dissipation	6
2.2.2	Mechanical dissipation	7
2.3	Dissipation mechanisms of mechanical Q	8
2.3.1	Anharmonic mechanisms	8
2.3.2	Fluidic damping	9
2.3.3	Material loss	10
2.3.4	Clamping loss	11
2.4	Photonic Crystals	13
2.4.1	Maxwell equations and the "master equation"	13
2.4.2	Lumerical	17
2.4.3	DBR mirror	17
3	Pillar Shaped Mechanical Devices	21
4	Photonic Crystal Membranes	25
4.1	Optical Characterization of Photonic Crystal Membranes	26
4.1.1	Photonic Crystal devices	26
4.1.2	Experimental Setup	26
4.1.3	Alignment Procedure	29
4.1.4	Wavelength dependent optical characterization	34
4.1.5	Normalized measurements at a fixed wavelength	43
4.2	Mechanical Characterization of Photonic Crystal Membranes	46
4.2.1	Experimental setup	46
4.2.2	Alignment procedure	48
4.2.3	Measuring and evaluation methods	49
4.2.4	Results	52
4.3	Summary	54
5	Quality Factors of Siliconnitride Membranes	55
5.1	SiN Membranes	55

Contents

5.2	Experimental Setup, Alignment, Measuring and Evaluation	55
5.2.1	Various holders and clampings	56
5.3	Results	58
5.3.1	Several SiN membranes under equivalent conditions	58
5.3.2	SiN membrane 10, comparison of all measurements	59
5.3.3	Comparison of Q of SiN membranes at room and low temperature	62
5.4	Summary	66
6	Conclusion and Outlook	67

1 Introduction

In recent years, there has been a rapidly growing interest in the field of cavity (quantum) optomechanics, which explores the coupling of the motion of a mechanical oscillator to the intensity of a cavity light field via radiation pressure.

Cavity optomechanical systems are employed in experiments going in three directions, namely quantum information, sensing applications and macroscale quantum mechanics.

For quantum information processing, it is necessary to interconvert flying photons and stationary qubits, e.g. spins in a magnetic material or charges on a conducting surface. One possibility to couple those in a direct way incompatible systems would be the use of a mechanical resonator as an interface between photons and qubits, i.e. the mechanical element serves as a light-matter transducer (as theoretically proposed e.g. in ref. [2]). An experiment towards this direction that has been realized is ref. [4], where ultracold atoms are coupled to a micromechanical membrane via a laser beam.

In the application of optomechanical systems for the detection of small forces, displacements, masses, and accelerations a prominent example is the atomic force microscope with force sensitivities exceeding $10^{-18} \text{N Hz}^{-1/2}$ (ref. [5]).

Finally, optomechanical systems are a good candidate to answer fundamental questions of quantum theory, like if there is a borderline between the macroscopic classical world and the microscopic quantum world. If there exists no boundary, then only decoherence prevents us from seeing quantum effects in our daily life (ref. [39]). Other theories predict non-linear extensions of the Schrödinger equation (ref. [40]), or a collapse of the wavefunction due to gravitational effects (ref. [41]). Creating genuine quantum states with resonators of increasing size demonstrates the validity of quantum mechanics for larger and larger scales.

In all the experiments in these fields, the mechanical element plays a crucial role. It has to exhibit excellent optical properties, allowing for good coupling between the light field and the mechanical resonator, and at the same time must have excellent mechanical properties, guaranteeing that the system is isolated from the environment as well as possible. How good the optical and mechanical properties are, can be expressed by the optical and mechanical quality factor. They are the sum of the inverse of the different losses. Light losses result from the input and output coupling of the light at the cavity mirrors, and from scattering and absorption losses inside the cavity. Losses directly related to the mechanical resonator

1 Introduction

are resulting from residual gas in the environment, effects in the resonator itself induced by deformation, and the clamping of the device.

There do already exist various types of mechanical resonators of different designs and materials, like for instance microtoroidal resonators (ref.[1]), beam-shaped resonators (ref. [8], [43]) and levitated spheres (ref. [44]). But the search for even better devices does not end.

The aim of this thesis is the investigation of the optical and mechanical properties of three optomechanical devices, which should exhibit lower losses than previous ones. The explored structures are newly shaped DBR (distributed Bragg reflector) mirror resonators, commercial silicon nitride membranes and silicon nitride photonic crystal membranes.

In chapter 2 of this thesis, the basic theoretical background of optomechanical systems, optical and mechanical dissipation, and photonic crystals is given. In chapter 3, we will give a short description of the DBR pillar structures, which should fulfil both requirements, good optical and mechanical properties. Another such device are photonic crystal membranes. Chapter 4 contains the experimental results of their reflectivity and the measurements of their mechanical quality factors. Chapter 5 finally focuses on the mechanical quality factors of commercial silicon nitride membranes for various methods of clamping.

2 Theory

2.1 Optomechanical Systems

2.1.1 Basic principle

First, we want to give a short explanation of the working principle (also see ref. [36], [37], [38]) of optomechanical systems and a rough idea of how they can be described mathematically.

The most basic situation is light hitting a movable mirror. The photons hitting the mirror and bouncing back transfer twice their momentum to the mirror, $\Delta p = 2 \frac{\hbar \omega_{light}}{c}$ with ω_{light} the light frequency, i.e. they exert a force on the mirror, the radiation pressure force. If the mirror has low mass and good mechanical properties, it can be approximated for small amplitudes as a harmonic oscillator with frequency ω_m and damping γ_m .

In order to enhance the coupling between light and mechanics, a second mirror is added (see fig. 2.1), such that the photons are reflected back and forth between the two mirrors and a cavity is built. That means that the light-matter interaction takes place many times until the light decays out of the cavity with a decay rate κ . The research field that focuses on light-matter coupling enhanced by optical cavities is called cavity optomechanics.

Cavity optomechanical systems can be realized in various ways. The setup described before corresponds to the configuration of one rigid mirror, the input coupler, and one movable mirror. This configuration, where the movable cavity mirror device fulfils both the optical and the mechanical function, is called reflective optomechanics. This is the setup our pillar structures and free-free devices are made for (see chapter 3).

An alternative is the separation of the mechanical and the optical function of the movable end mirror, called dispersive optomechanics. In this case, the high reflectivity, which is necessary to create a working cavity, is achieved by using a second *rigid* cavity end mirror fulfilling the optical part, whereas the mechanical part is transferred to an extra device, e.g. a membrane that is mounted inside the cavity. Possible membranes employed for the implementation of such a system will be investigated in chapter 5.

The coupling of light with a membrane in a cavity can be improved by using membranes with higher reflectivity, which might be achieved by the last optomechanical

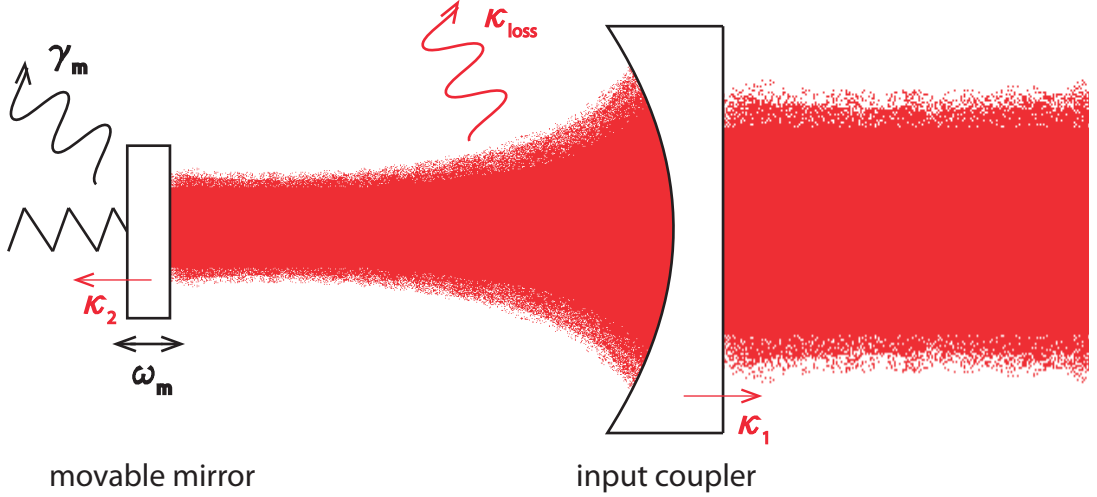


FIGURE 2.1: **Principle of cavity optomechanics.** Light couples to the movable mirror via radiation pressure. The resulting effects can be enhanced by adding a second mirror, the input coupler, to build a cavity. The mirror, oscillating with the mechanical frequency ω_m of mode m , is damped by coupling to the thermal environment with the coupling constant γ_m . The incoherent optical losses through absorption and scattering are indicated by κ_{loss} . κ_1 and κ_2 are the losses at the two mirrors originating from in- and out-coupling. They can be measured in principle.

device treated in this work, silicon nitride photonic crystal membranes. If they do not only have excellent mechanical properties, but also high reflectivities (estimation see 2.2.1), they might be even used as cavity end mirrors in a setup similar to the first one described here.

2.1.2 Basic mathematical description of the system

Here, the most important ideas of the mathematical description of an optomechanical system are summarized in order to give an idea how the coupling g and the dissipation factors κ and γ_m , that will be needed in the following, are rooted in the theoretical apparatus of quantum optomechanics. For a comprehensible more detailed overview, see ref. [7]. A detailed discussion is given in ref. [6].

For the description of the system, we start with its **Hamiltonian**.

The free motion of the light and the mechanical oscillator (for small amplitudes of the oscillator) can be well approximated by two harmonic oscillators, i.e. the Hamiltonian reads $\hat{H}_{free} = \hbar\omega_{cav,0}\hat{a}^\dagger\hat{a} + \hbar\omega_m\hat{b}^\dagger\hat{b}$, where $\omega_{cav,0}$ is the resonance frequency of the rigid cavity, \hat{a}^\dagger/\hat{a} are the intracavity photon creation/annihilation operators, and \hat{b}^\dagger/\hat{b} are the phonon creation/annihilation operators.

In a next step, the light-matter interaction is included by taking into account that

- due to the motion of the oscillator with frequency ω_m - the cavity resonance frequency $\omega_{cav}(\hat{x})$ permanently changes, depending on the oscillator's position. The actual $\omega_{cav}(\hat{x})$ can be approximated by $\omega_{cav}(\hat{x}) \approx \omega_{cav,0} + \frac{\partial \omega_{cav}(x)}{\partial x} \hat{x}$. This leads to the following expression for the Hamiltonian \hat{H}_{lm} that includes the uncoupled terms and the non-linear interaction term

$$\hat{H}_{lm} = \hbar \omega_{cav,0} \hat{a}^\dagger \hat{a} + \hbar \omega_m \hat{b}^\dagger \hat{b} + \hbar \frac{\partial \omega_{cav}(x)}{\partial x} \hat{a}^\dagger \hat{a} \hat{x}. \quad (2.1)$$

Here, $\hat{x} = x_{zp}(\hat{b} + \hat{b}^\dagger)$ is the position operator of the mechanical device with the zero-point fluctuation $x_{zp} = \sqrt{\frac{\hbar}{2m_{eff}\omega_m}}$ and the effective mass m_{eff} .

Since the last term represents the interaction, it is plausible to define the single-photon coupling rate of a photon to the mechanical resonator as $g_0 = \frac{\partial \omega_{cav}(x)}{\partial x} x_{zp}$. One can see that the single-photon coupling in a cavity of certain length can be increased by reducing the effective mass of the resonator or by working with a lower mechanical resonance frequency. In a cavity, there usually is not one single photon but many, so the coupling between the entire intracavity field and the mechanics reads $g = g_0 \sqrt{\bar{n}_{cav}}$ after a linearization of the Hamiltonian, with \bar{n}_{cav} the mean intracavity photon number.

In order to cover a realistic system, the Hamiltonian has to be extended by some terms. It must take account of the external driving laser (which is needed to maintain the cavity photon field), of photon losses denoted by the cavity decay rate κ , and phonon dissipation due to the coupling of the mechanical device to a thermal bath with a damping rate γ_m . The full description of the time evolution of an optomechanical system is given by equations of motion that have the form of Langevin equations (for a derivation see ref. [6]).

The basis for the quantum Langevin equations are the Heisenberg equations of motion, $\frac{dY}{dt} = \frac{i}{\hbar}[H, Y]$ for an arbitrary system operator Y , containing the full Hamiltonian, H , inclusively the additional terms listed before.

The Langevin equations for the cavity field amplitude \hat{a} and the mechanical amplitude \hat{b} are given by [11]

$$\frac{d\hat{a}}{dt} = -\frac{\kappa}{2}\hat{a}(t) + i(\Delta - \frac{g_0}{x_{zp}}\hat{x}(t))\hat{a}(t) + \sqrt{\kappa_{in}}\hat{a}_{in}(t) + \sqrt{\kappa_{loss}}\hat{a}_{vac}(t) \quad (2.2)$$

$$\frac{d\hat{b}}{dt} = (-i\omega_m - \frac{\gamma_m}{2})\hat{b}(t) + ig_0\hat{a}^\dagger(t)\hat{a}(t) + \sqrt{\gamma_m}\hat{b}_{in}(t). \quad (2.3)$$

These equations are valid after switching into the rotating frame of the external laser at frequency ω_{laser} . This entails a transformation of the light field operator according to $\hat{a}_{old} \rightarrow \hat{a}_{new} \exp[-i\omega_{laser}t]$ and an altered form of the Hamiltonian. The expression $\Delta = \omega_{laser} - \omega_{cav,0}$ is also a result of the rotating frame picture. The cavity decay rate $\kappa = \kappa_{in} + \kappa_{loss}$ comprises two parts, the photon decay from

2 Theory

the input and output coupling, $\kappa_{in} = \kappa_1 + \kappa_2$, and the intracavity photon losses, κ_{loss} . γ_m is the damping rate of the oscillator with frequency ω_m , originating from the coupling to the thermal bath with the field operator $\hat{b}_{in}(t)$. κ and γ_m will be treated in more detail in section 2.2. $\hat{a}_{in}(t)$ is the field operator of the input laser field, and $\hat{a}_{vac}(t)$ of the vacuum field.

By adding the correlators of $\hat{a}_{in}(t)$ and $\hat{b}_{in}(t)$ to the Langevin equations, the time evolution of the photon field and the mechanical device is completely described.

$$\langle \hat{a}_{in}(t) \hat{a}_{in}^\dagger(t') \rangle = \delta(t - t') \quad (2.4)$$

$$\langle \hat{a}_{in}^\dagger(t) \hat{a}_{in}(t') \rangle = 0 \quad (2.5)$$

$$\langle \hat{b}_{in}(t) \hat{b}_{in}^\dagger(t') \rangle = (\bar{n}_{th} + 1) \delta(t - t') \quad (2.6)$$

$$\langle \hat{b}_{in}^\dagger(t) \hat{b}_{in}(t') \rangle = \bar{n}_{th} \delta(t - t') \quad (2.7)$$

The second equation is valid for the approximation of zero thermal occupation number of the optical field due to the high frequency of the light, i.e. $k_B T / \hbar \omega \approx 0$.

2.2 Optical and Mechanical Dissipation

2.2.1 Optical dissipation

2.2.1.1 Optical quality factor

The quality of an optical cavity is determined by the reflectivities of its mirrors and its internal photon loss rate. Therefore, the **optical quality factor** is defined as

$$Q_{opt} = \omega_{cav,0} \tau, \quad (2.8)$$

where $\omega_{cav,0}$ is the resonance frequency of the cavity, and τ the photon lifetime with $\tau^{-1} = \kappa$ the cavity decay rate from before.

As mentioned before, $\kappa = \kappa_{loss} + \kappa_1 + \kappa_2$ for a high-Q optical cavity. $\kappa_1 + \kappa_2 = \kappa_{in}$ represent the losses due to the in- and out-coupling of the intracavity field to the external driving field modes, and κ_{loss} is the photon decay due to absorption and scattering inside the cavity, which cannot be measured.

2.2.1.2 Finesse

Another important optical quantity is the **finesse**, F , corresponding to the number of round-trips a photon in the cavity makes before it decays. It is defined by the ratio of the free spectral range $\Delta\omega_{FSR}$, which is the frequency difference between two cavity resonance frequencies, and κ (half-width-at-half-maximum),

$$F = \frac{\Delta\omega_{FSR}}{2\kappa}. \quad (2.9)$$

A different way of writing the finesse contains the reflectivity of the mirrors and therefore shows the connection between the cavity decay rate and the reflectivity. For $r_1, r_2 \rightarrow 1$ it is given by

$$F = \frac{\pi \sqrt{r_1 r_2}}{1 - r_1 r_2} \quad (2.10)$$

with r_1, r_2 the amplitude reflectivities of mirror 1, 2.

2.2.1.3 Estimations for photonic crystal membranes as end-mirrors

In order to clarify if the photonic crystal membranes could possibly be used as end-mirror in a cavity, their required reflectivity r_1 is estimated.

For many optomechanical experiments sideband resolution is required, giving the condition

$$\frac{\kappa}{2\omega_m} < 1. \quad (2.11)$$

Inserting the free spectral range $\Delta\omega_{FSR} = \pi \frac{c}{L}$ for a Fabry-Pérot cavity into equ. 2.9 and plugging the κ resulting from this equation into the resolved-sideband condition (equ. 2.11) yields

$$F > \frac{\pi c}{2\omega_m L} \approx 7.5 \times 10^3 \quad (2.12)$$

with c the speed of light, the mechanical frequency $\omega_m = 2\pi \times 1MHz$, and $L = 10^{-2}m$. Inserting this into equ. 2.10 with $r_2 \approx 1$ results in a required amplitude reflectivity of $r_1 = 0.9996$ and an intensity reflectivity of $R_1 = |r_1|^2 = 0.9992$ for the photonic crystal membrane.

2.2.2 Mechanical dissipation

In analogy to the optical quality factor, a mechanical quality factor is defined as

$$Q_m = \frac{\omega_m}{\gamma_m} \quad (2.13)$$

for the mechanical mode m .

The mechanical Q-factor is inversely proportional to γ_m , the mechanical damping rate, also called energy dissipation rate. γ_m describes the coupling of the mechanical oscillator to its environment, a classical thermal bath of temperature T_{bath} , which can be described as an assembly of harmonic oscillators with occupation number \bar{n}_{th} . Due to the coupling to the thermal bath, the state of the mechanical oscillator evolves into a classical state with time. Therefore, to enable quantum experiments, the coherent interaction between the light and the mechanical oscillator must be much stronger than the incoherent interaction of the oscillator to the thermal bath, i.e. $g \gg \bar{n}_{th}\gamma_m$.

$\bar{n}_{th}\gamma_m$ is called **thermal decoherence rate** and - assuming the resonator initially being in its ground state - is given by

$$\bar{n}_{th}\gamma_m \approx \frac{k_B T_{bath}}{\hbar Q_m} \quad (2.14)$$

with k_B being the Boltzmann constant.

From this equation one can see that low temperatures and high mechanical Q-factors reduce the thermal decoherence rate. Low temperature is usually achieved by cooling the setup in a cryostat. Ways how to experimentally achieve high mechanical Q-factors are discussed elaborately in this thesis. The different dissipation mechanisms causing high damping and low Q-factors will be treated in chapter 2.3.

A frequently used parameter for the mechanical quality of a system is the " $Q \cdot f$ " **product**. It explicitly takes into account the frequency and indicates how well the mechanical oscillator is decoupled from its thermal environment. For example, the number of coherent oscillations in the presence of thermal decoherence, $\frac{\omega_m}{\bar{n}_{th}\gamma_m} = Q_m f_m \frac{\hbar}{k_B T}$, is proportional to the $Q \cdot f$ product.

2.3 Dissipation mechanisms of mechanical Q

There are four major loss mechanisms summing up to the parameter of interest, the total dissipation. They are thermoelastic damping (TED), fluidic damping, dissipation due to the material properties, and clamping losses. For non-coupled losses, of the contributions can be expressed by the reciprocal of the corresponding Q-factor

$$\frac{1}{Q} = \frac{1}{Q_{TED}} + \frac{1}{Q_{fluidic}} + \frac{1}{Q_{material}} + \frac{1}{Q_{clamping}}. \quad (2.15)$$

2.3.1 Anharmonic mechanisms

The first class of damping mechanisms treats the internal consequences of the flexure of the oscillator. Anharmonic mechanisms include thermoelastic damping and the Akhiezer effect.

Thermoelastic damping In silicon nitride the dominating anharmonic effect is thermoelastic damping. When the resonator is bent during its oscillation, one surface is compressed while the opposite one is expanded. This results in an increase and decrease of temperature, respectively, as the strain field in a thermoelastic solid is coupled to the temperature field via a coupling constant, the thermal expansion coefficient α . The linear thermal expansion coefficient for a device of length L and temperature T reads $\alpha = \frac{1}{L} \frac{\partial L}{\partial T}$, and is valid in an isotropic solid with a thermalization rate that is high enough that the device thermalizes before being bent again in the opposite direction. The corresponding volumetric thermal expansion coefficient

is 3α . To relax back to thermal equilibrium from the situation of one surface being colder and the other hotter, heat is transferred through the resonator. This flow increases the entropy and involves internal friction, i.e. energy losses.

The strength of the thermodynamical damping depends on the oscillation frequency ω of the beam. For high frequencies $\omega \gg \tau^{-1}$, with τ being the time the oscillator needs to fully thermalize, therefore τ^{-1} being the thermalization rate, there will be almost no heat transfer because the compressed (hence heated) surface is expanded (hence cooled) again before the heat could propagate and vice-versa for the second surface, i.e. the vibration proceeds adiabatically, without heat exchange.

On the other hand, vibrations at low frequencies, $\omega \ll \tau^{-1}$, are isothermal, which means that they do not result in energy dissipation either.

The dissipation due to thermoelastic damping is at its maximum when $\omega \approx \tau^{-1}$, i.e. the time the system needs for thermalization is about the time one period of oscillation takes.

For further information see ref. [9], [10], [11], [12].

For high-stress SiN membranes one can apply

$$Q_{TED} = 12 \frac{(1 - \nu)^2 C_p \sigma^2}{(2\pi f_m)^2 E^2 \alpha^2 T t^2} \frac{1}{g(\xi)}, \quad (2.16)$$

where

$$g(\xi) = -\frac{6 \sinh \xi + \sin \xi}{\xi^3 \cosh \xi + \cos \xi} + \frac{6}{\xi^2}, \quad (2.17)$$

and $\xi = t \sqrt{\frac{2\pi f_m \rho C_p}{2\kappa}}$, with Poisson's ratio $\nu = 0.27$, specific heat $C_p = 700$ J/(kg K), tensile stress $\sigma = 0.8$ GPa, mode frequency $f_m = 1$ MHz, Young's modulus $E = 260.5$ GPa, coefficient of thermal expansion $\alpha = 2 \times 10^{-6}$ K $^{-1}$, equilibrium temperature $T = 293$ K, membrane thickness $t = 50$ nm, density of high-stress silicon nitride $\rho = 2.7$ g/cm 3 , and thermal conductivity $\kappa = 20$ W/(m K).

Inserting the numbers relevant for our experiment in equ. 2.16 we get $Q_{TED} \approx 10^{16}$, which means that thermoelastic damping is not the limiting effect for high-stress SiN membranes.

Akhiezer effect: Strain resulting from anharmonicity in the material modulates the phonon frequencies of the mechanical modes differently for each mode. This leads to a distortion of the initial phonon distribution, and takes time and energy to reestablish phonon equilibrium. This effect is described in ref. [13], [45], [46].

2.3.2 Fluidic damping

Damping from the interaction of the resonator with the surrounding fluidic medium occurs in three different ways (ref. [14], [15] - acoustic radiation (ref. [47]), viscous

drag, and the squeeze-film effect.

Acoustic radiation is an important loss mechanism for planar sources vibrating out-of-plane. The oscillation induces acoustic waves that are irradiated with a certain energy. As the dissipated energy scales linearly with the pressure of the surrounding gas, this mechanism can be neglected in our case, where we operate under low pressures around 10^{-5} mbar. Squeeze-film damping appears, when a thin layer of the surrounding medium is compressed between the moving plate and another solid element close to it. The medium then damps or amplifies the motion of the moving plate. This effect is not relevant for us.

Viscous damping, on the contrary, plays a non-negligible role in our system. By operating in vacuum, this source of damping can be reduced to a negligible effect for the current devices. But it might soon be important to operate under even lower pressures as the limit for the quality factor set by viscous damping at the current pressure is of the order of 10^8 .

For high-stress SiN membranes, the following formula is used for estimations of the limitation by viscous damping (ref. [16])

$$Q_{fluidic}(p) = \left(\frac{\pi}{2}\right)^{\frac{3}{2}} \rho t f_m \sqrt{\frac{k_B T}{m}} \frac{1}{p}, \quad (2.18)$$

where the density of high-stress SiN $\rho = 2.7 \text{ g/cm}^3$, the mode frequency $f_m = 1 \text{ MHz}$, the thickness of the membrane $t = 50 \text{ nm}$, the Boltzmann constant $k_B = 1.38 \times 10^{-23} \text{ J/K}$, and the molecular mass $m = \frac{29 \times 10^{-3}}{6 \times 10^{23}} \text{ g}$.

At room temperature $T = 293 \text{ K}$, the pressure is $p = 5 \times 10^{-5} \text{ mbar}$, which results in $Q_{fluidic} \approx 1.5 \times 10^7$. This is quite low and almost seems to be a limiting factor for our quality factors. Nevertheless, at the moment the other losses, e.g. clamping losses (see 2.3.4), seem to be dominant as we never reach Q-factors beyond $Q \approx 2 \times 10^6$. But with better clamping this might set a limit to the quality factor of the membranes.

At low temperatures, $Q_{fluidic}$ is raised to $Q_{fluidic} \approx 2.5 \times 10^8$, which makes it negligible, considering that the highest values measured for the mechanical quality factor of the SiN membranes were lower than 10^8 . The enhancement of Q with T is not immediately clear when looking at equ. 2.18. One can see that lower T decreases $Q_{fluidic}$, but we observed a drop in pressure to $p \approx 3 \times 10^{-6} \text{ mbar}$ during operation at cryogenic temperatures as residual gas was frozen out by the flowing Helium. This caused the higher value for $Q_{fluidic}$.

2.3.3 Material loss

Another mechanism of damping relies on localized defects of the resonator medium itself. These defects can be extrinsic, i.e. impurities, or intrinsic, i.e. lattice atoms being on the wrong position, disturbing the periodic crystal structure. Extrinsic defects can be eliminated by growing high purity crystals, whereas intrinsic defects

will always appear because of energy minimization. The defects can be located in the bulk as well as on the surface of the structure. They are mostly explained by the standard tunneling model, where the phonons of the resonator modes couple dissipatively to the defects, which are modeled as two-level systems (TLS), i.e. they exhibit two energy minima separated by an energy barrier. For more detailed information see ref. [17], [18], [19], [20], [42].

Material dissipation becomes the dominating loss effect at low temperatures for resonators of decreasing size. In our case, they can be neglected as the dominating loss mechanism still are the clamping losses.

2.3.4 Clamping loss

Clamping or anchor losses are theoretically and experimentally discussed in ref. [8], ref. [21]-ref. [25].

The mechanical devices in an experiment have to be held in place. In levitating systems using e.g. nanospheres as mechanical devices (ref. [44]), the trapping is done by a laser beam, which means that no solid connection to a supporting substrate is necessary. In non-levitating systems, the solid connection of the structure to its support is always needed, which results in dissipation of mechanical energy into the support material, called phonon-tunneling. This effect exhibits a strong geometrical dependence, it is for example highly influenced by the position of the clamping of the membrane to the support material.

2.3.4.1 Free-free structures

A kind of device that we are going to touch in this thesis are "free-free" micro-mechanical structures, described in ref. [8]. These resonators are beam-shaped plates that are suspended by four thin auxiliary beams (see 2.2). The name "free-free" comes from the fact that the central beam is not fixed at its ends but somewhere along its long side, such that the ends can oscillate freely. By varying the position at which the auxiliary beams attach to the central resonator, the geometric character of the clamping losses can be demonstrated and the clamping losses can be investigated separately, while the other parameters, such as temperature, resonator length (and therefore resonance frequencies) and surface-to-volume ratio remain approximately constant. It was shown (experimentally and theoretically) that the minimal losses are obtained when the auxiliary beams are attached at the nodes of the fundamental mode of the resonator, that means that when the auxiliary beams move less, they transfer less energy to the substrate.

A variation of the free-free structures was designed in the course of this work and shall be described in chapter 3.

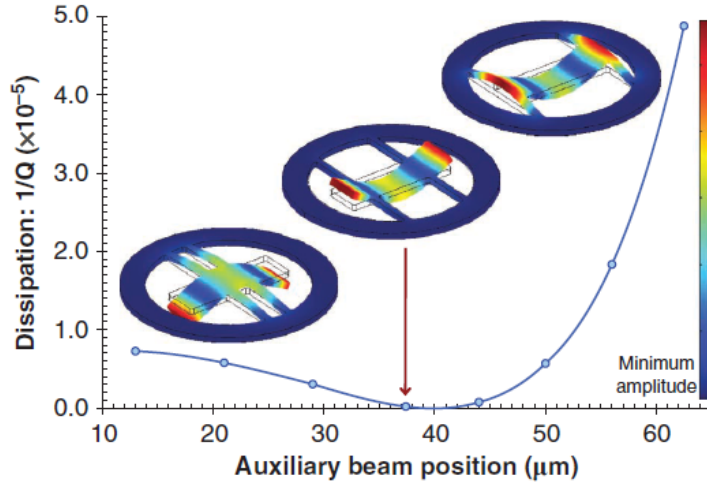


FIGURE 2.2: **Free-free structures.** These simulations show the dependence of the clamping losses on the position of the auxiliary beams. With the beams attached to the nodes of the resonator eigenmodes, minimal coupling to the environment is achieved. (Figure courtesy of G.Cole ref. [8].)

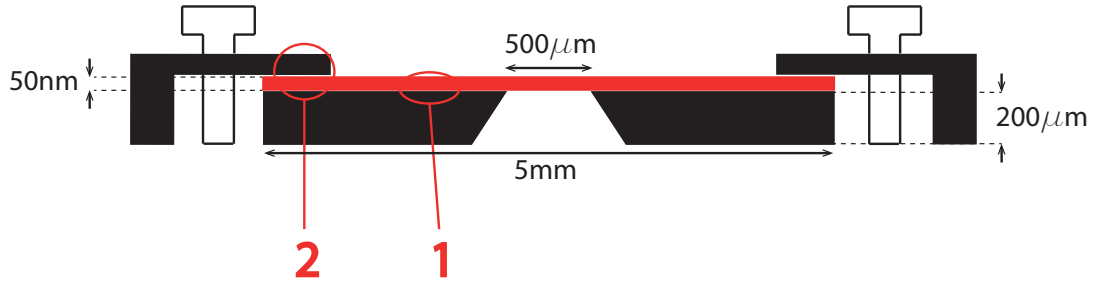


FIGURE 2.3: Clamped SiN Norcada chip. Losses arise at two points. (1) losses from the SiN membrane to the Si frame, (2) losses from the whole chip to the holder via clamping.

2.3.4.2 High-stress SiN membranes

The clamping loss mechanism of stoichiometric SiN Norcada membranes, that are discussed in this thesis, has been simulated and tested experimentally in ref. [25]. The Norcada devices consist of an e.g. 100nm thick SiN membrane layer that is directly placed on a 200 μ m thick Si frame with a window in the middle which defines the actual membrane (see fig. 2.3). In ref. [25], it was found that the anchor losses from the membrane to the Si substrate exceed fluidic, thermoelastic and material dissipation and are therefore the most relevant loss mechanism for the SiN membranes.

For the SiN membranes, clamping losses arise at two points (see fig. 2.3). The first (1) is the contact between the membrane and the Si frame, which is predefined by the company and cannot be improved afterwards. These effects were explored in ref. [25]. The second point (2) is the way of clamping the chip to a holder, which is determined by the experimentalist. This is what we investigated in the experiments that are presented in this work, and what we are going to refer to as "clamping" of the membranes from now on.

In summary, it can be said that for the systems investigated in this thesis, the dissipation by clamping is the limiting loss mechanism, while thermoelastic effects are negligible, fluidic damping is strongly reduced by operating in vacuum, and material losses do not occur to a great extent.

2.4 Photonic Crystals

In this chapter, the rough background for photonic crystal membranes shall be discussed. This implies an overview of the mathematical treatment of photonic crystals based on the Maxwell equations, a short description of how the simulations of the wavelength-dependent reflectivities for our membranes were performed, and the working principle of DBR mirrors, as they are 1-dimensional photonic crystals and the mirrors currently used in optomechanics experiments. The first part of the introduction follows ref. [27], which is also recommended for more detailed information.

2.4.1 Maxwell equations and the "master equation"

Photonic crystals are low-loss periodic dielectric media, whose periodicity is obtained by arranging two materials with a high contrast in refractive index in a 1-, 2-, or 3-dimensional periodic way. DBR mirrors are the easiest 1-dimensional example of photonic crystals. The propagation of light in a photonic crystal works analog to electrons propagating as waves in a crystal lattice, like e.g. in semiconductors, where electrons are subjected to the periodic potential of the lattice atoms. The idea is that photonic crystals could be a new means to control light in a better way. Similar to the electronic case, photonic crystals can be designed to have a

2 Theory

complete photonic band gap, i.e. for a certain frequency range, the photonic crystal prohibits the propagation of electromagnetic waves of any polarization in any direction. In this case, all the incoming light is reflected, which is the effect used to reach the high reflectivities of our photonic crystal membranes.

The mathematical description of light propagating through dielectric media is based on the **Maxwell equations**

$$\nabla \cdot \mathbf{B} = 0 \quad (2.19)$$

$$\nabla \times \mathbf{E} + \frac{\partial \mathbf{B}}{\partial t} = 0 \quad (2.20)$$

$$\nabla \cdot \mathbf{D} = \rho \quad (2.21)$$

$$\nabla \times \mathbf{H} - \frac{\partial \mathbf{D}}{\partial t} = \mathbf{J} \quad (2.22)$$

where \mathbf{E} and \mathbf{H} are the electric and magnetic fields, respectively, \mathbf{D} and \mathbf{B} are the electric displacement and magnetic induction fields, and ρ and \mathbf{J} are the free charge and current densities.

The relation between \mathbf{D} and \mathbf{E} is given by

$$\frac{D_i}{\epsilon_0} = \sum_j \epsilon_{ij} E_j + \sum_{jk} \chi_{ijk} E_j E_k + O(E^3), \quad (2.23)$$

where $\epsilon_0 \approx 8.854 \times 10^{-12} \text{ F/m}$ is the vacuum permittivity, ϵ_{ij} is the first order susceptibility, and χ_{ijk} is the second order susceptibility.

Making several assumptions, the relation 2.23 simplifies to $\mathbf{D}(\mathbf{r}) = \epsilon_0 \epsilon(\mathbf{r}) \mathbf{E}(\mathbf{r})$. The first assumption is small field strengths, so that the non-linear terms can be neglected. The others are that the material be macroscopic, isotropic, and transparent, further the system is considered in a small frequency range. Then ϵ_{ij} becomes the scalar, real, positive, and frequency independent relative permittivity $\epsilon(\mathbf{r})$.

Similarly, for the magnetic field the relation $\mathbf{B} = \mu_0 \mathbf{H}$ holds, with the vacuum permeability $\mu_0 = 4\pi \times 10^{-7} \text{ H/m}$, taking into account that for most dielectric materials the relative magnetic permeability $\mu(\mathbf{r})$ is close to unity at optical frequencies.

With these assumptions and the fact that there are no light sources in the material under consideration, the Maxwell equations read

$$\nabla \cdot \mathbf{H}(\mathbf{r}, t) = 0 \quad (2.24)$$

$$\nabla \times \mathbf{E}(\mathbf{r}, t) + \mu_0 \frac{\partial \mathbf{H}(\mathbf{r}, t)}{\partial t} = 0 \quad (2.25)$$

$$\nabla \cdot \epsilon(\mathbf{r}) \mathbf{E}(\mathbf{r}, t) = 0 \quad (2.26)$$

$$\nabla \times \mathbf{H}(\mathbf{r}, t) - \epsilon_0 \epsilon(\mathbf{r}) \frac{\partial \mathbf{E}(\mathbf{r}, t)}{\partial t} = 0. \quad (2.27)$$

As the Maxwell equations are linear partial differential equations, a **Fourier ansatz** can be made that separates the time from the spatial dependence by expanding the field into a set of **harmonic modes** of the form

$$\mathbf{H}(\mathbf{r}, t) = \mathbf{H}(\mathbf{r}) \exp[-i\omega t] \quad (2.28)$$

$$\mathbf{E}(\mathbf{r}, t) = \mathbf{E}(\mathbf{r}) \exp[-i\omega t]. \quad (2.29)$$

Inserting equ. 2.29 into equ. 2.27, from the divergence equations, there follow the conditions

$$\nabla \cdot \mathbf{H}(\mathbf{r}) = 0 \quad (2.30)$$

$$\nabla \cdot \epsilon(\mathbf{r}) \mathbf{E}(\mathbf{r}) = 0. \quad (2.31)$$

Similarly, there follow conditions for the curl equations, which can be decoupled to eventually one "master equation" that is entirely in $\mathbf{H}(\mathbf{r})$,

$$\nabla \times \left(\frac{1}{\epsilon(\mathbf{r})} \nabla \times \mathbf{H}(\mathbf{r}) \right) = \left(\frac{\omega}{c} \right)^2 \mathbf{H}(\mathbf{r}). \quad (2.32)$$

The "**master equation**" 2.32, together with the divergence equation 2.30, contains all the necessary information about $\mathbf{H}(\mathbf{r})$. Knowing $\epsilon(\mathbf{r})$, the master equation can be solved, i.e. the modes $\mathbf{H}(\mathbf{r})$ with the corresponding frequencies ω are calculated. From the relation between $\mathbf{H}(\mathbf{r})$ and $\mathbf{E}(\mathbf{r})$, the electrical field $\mathbf{E}(\mathbf{r})$ is deduced. This is the desired full description of the modes and the frequencies of the light field.

In order to find the solutions of the "master equation", its consideration as an **eigenvalue problem** is useful. The Hermitian operator $\hat{\Theta}$ acting on the function $\mathbf{H}(\mathbf{r})$ gives a constant, called the eigenvalue, times the function itself, called eigenvector, i.e.

$$\hat{\Theta} \mathbf{H}(\mathbf{r}) = \left(\frac{\omega}{c} \right)^2 \mathbf{H}(\mathbf{r}) \quad (2.33)$$

with $\hat{\Theta} \mathbf{H}(\mathbf{r}) = \nabla \times \left(\frac{1}{\epsilon(\mathbf{r})} \nabla \times \mathbf{H}(\mathbf{r}) \right)$.

The periodicity of the photonic crystals can be used to find a simpler form of the "master equation". The **Bloch theorem** states that the mode shape in the presence of discrete translational symmetries in the crystal can be expressed by a plane wave modulated by a periodic function. For a 3-dimensional structure, the Bloch theorem reads

$$\mathbf{H}_{\mathbf{k}}(\mathbf{r}) \propto \exp[i\mathbf{k}\mathbf{r}] \mathbf{u}_{\mathbf{k}}(\mathbf{r}). \quad (2.34)$$

Inserting equ. 2.34 into the eigenvalue problem equ. 2.33 gives the new "master equation" in \mathbf{k} ,

$$\hat{\Theta}_{\mathbf{k}} \mathbf{u}_{\mathbf{k}}(\mathbf{r}) = \left(\frac{\omega(\mathbf{k})}{c} \right)^2 \mathbf{u}_{\mathbf{k}}(\mathbf{r}), \quad (2.35)$$

with $\hat{\Theta}_{\mathbf{k}} = (i\mathbf{k} + \nabla) \times \frac{1}{\epsilon(\mathbf{r})} (i\mathbf{k} + \nabla) \times$.

2.4.1.1 Band structure diagrams

From equ. 2.35, ω and \mathbf{k} are calculated, and a band structure diagram $\omega(k)$ can be drawn. Fig. 2.4 shows the band diagram for a structure with 2-dimensional discrete translational periodicity, which is what we have for the photonic crystal membranes. When looking at fig. 2.4, one can see that for certain frequencies, there exists no \mathbf{k} in the $x - y$ plane, which means that the light of this frequency cannot propagate in the plane. This is called a band gap. The corresponding frequencies are the frequencies at which our membranes exhibit the highest reflectivities.

One can further see in fig. 2.4, that in 2-dimensional structures there are modes of two distinct polarizations, TE and TM modes. For TE (transverse-electric) modes, the electric field is confined to the $x - y$ -plane, i.e. (E_x, E_y, H_z) , while for TM (transverse-magnetic) modes the magnetic field is confined to the $x - y$ -plane, i.e. (H_x, H_y, E_z) . A complete band gap only occurs for frequencies at which both TE and TM modes have a band gap.

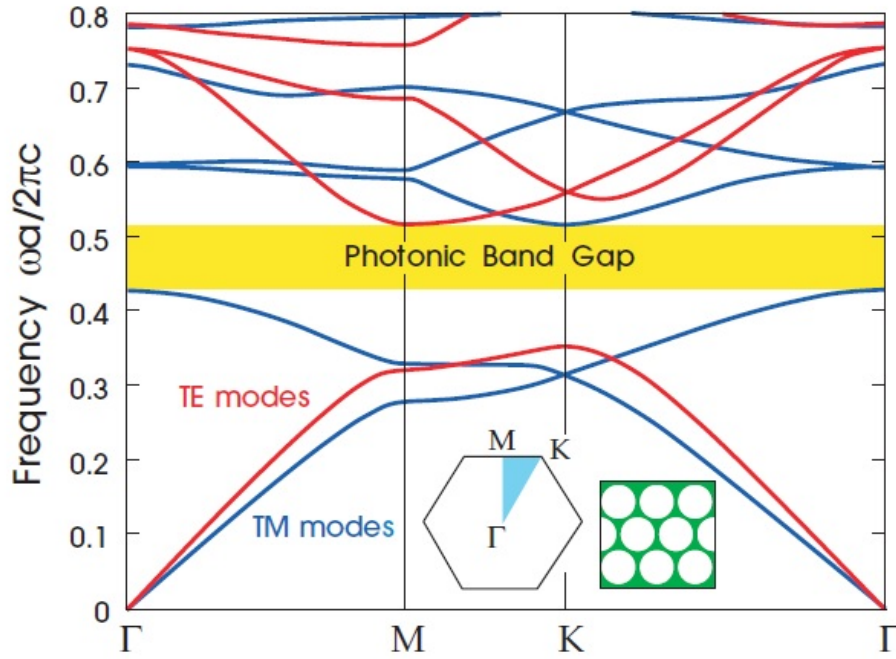


Figure 10: The photonic band structure for the modes of a triangular array of air columns drilled in a dielectric substrate ($\epsilon = 13$). The blue lines represent TM bands and the red lines represent TE bands. The inset shows the high-symmetry points at the corners of the irreducible Brillouin zone (shaded light blue). Note the complete photonic band gap.

FIGURE 2.4: Example of a **band structure diagram**. Figure courtesy of ref. [27].

2.4.2 Lumerical

In practice, the theoretical simulations of our photonic crystal structures (see 4.10 and 4.11) were performed with the program "lumerical", which is based on the finite-difference time-domain method (FDTD). This numerical analysis technique is suited for the treatment of electrodynamical systems by offering a way for solving the partial differential equations occurring there, like the Maxwell equations in our case. In the Maxwell equations, the change in time of the electric field \mathbf{E} depends on the change in space of the magnetic field \mathbf{H} , and conversely. In the FDTD analysis, the time development of the \mathbf{E} - and the \mathbf{H} -field is simulated separately for every volume element. The new value of \mathbf{E} is obtained from the stored value of \mathbf{E} and the curl of the local spatial distribution of \mathbf{H} . In the next step, the new value of \mathbf{H} in the same volume element for the next time step is calculated from the stored value of \mathbf{H} and the curl of the local spatial distribution of \mathbf{E} . Like that, one proceeds iteratively in time and obtains the electric and magnetic field evolution for every volume element.

With that knowledge, the reflectivities depending on the wavelength can be obtained.

2.4.3 DBR mirror

As already mentioned, DBR (distributed Bragg reflector) mirrors, also called dielectric mirrors, are 1-dimensional photonic crystals. In this section, we want to explain their working principle as they currently are the basic means to obtain high reflectivities needed in optomechanical experiments.

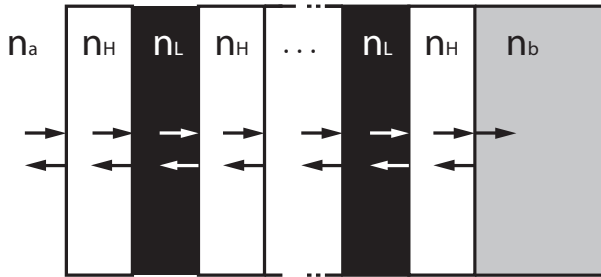


FIGURE 2.5: **DBR mirror.** At the boundary between two dielectric materials with a high contrast in refractive index n_H and n_L light is partly reflected and partly transmitted. By making a stack of several alternating layers each of thickness t_H and t_L such that the optical path length is $t_H n_H = \lambda/4 = t_L n_L$, constructive interference of all layers occurs, and exorbitantly high reflectivities can be achieved.

2 Theory

DBR mirrors are based on the fact that light traveling from one medium to another is partly reflected and partly transmitted at the boundary between the two media. The proportion of reflected and transmitted light can be deduced from Fresnel equations. They give the amplitude reflection and transmission dependent on the contrast of the refractive indices n_H and n_L of the media, and on the incident angle. For a perpendicularly incident beam, the angle dependence vanishes and Fresnel equations simplify to

$$r = \frac{n_H - n_L}{n_H + n_L} \quad (2.36)$$

for the amplitude reflection at fixed frequency. This means that, having two layers of different materials, the only way to enhance the amplitude reflection is choosing materials with a high contrast in refractive index. Since the refractive indices of most materials span only the range between 1 and 5, the achieved (intensity) reflectivity $R = |r|^2$ is limited at a rather low level. This restriction can be circumvented and almost arbitrarily high intensity reflectivities can be reached by not using only two layers of material but fabricating multilayer stacks of dielectric films.

A multilayer dielectric mirror consists of alternating layers of two materials with high and low refractive index, respectively. The number of layers has to be odd, and the outermost films are made of the high-index material.

The thickness t_H and t_L of the layers with high and low refractive index n_H and n_L is chosen such that $t_H n_H = \lambda/4 = t_L n_L$, i.e. the optical path length is a quarter of the wavelength λ of the incident beam. This allows for the high reflectivities as it causes constructive interference of the light reflected at each boundary.

At the first boundary, the incident light is partly reflected and partially transmitted. When the transmitted light hits the boundary to the next layer, it is again partly reflected and partially transmitted, and so on. Because of the optical thickness of $\lambda/4$ of the layers, there is a difference of $\lambda/2$ in the optical path length between the light reflected at two different boundaries. An additional difference of π in phase shift between the high-to-low and the low-to-high index boundary causes in total constructive interference of the reflected light from all layers.

The amplitude reflection of a dielectric Bragg mirror with N layers reads (ref. [26])

$$r = \frac{1 - \left(\frac{n_H}{n_L}\right)^{2N} \frac{n_H^2}{n_a n_b}}{1 + \left(\frac{n_H}{n_L}\right)^{2N} \frac{n_H^2}{n_a n_b}}, \quad (2.37)$$

where n_a and n_b are the refractive indices of the input and output medium, respectively. Usually, for our applications, the input medium is air ($n_a \approx 1$) and the output medium is the substrate on which the mirror was grown. Again, fixed light frequency is assumed, which leads to n_H and n_L independent of frequency, and the thickness of the mirror layers does not appear in the formula as it is assumed to be such that the optical path length is a quarter of the light wavelength.

One can see from the above equation, that for a higher difference in n_H and n_L ,

$r \rightarrow -1$, and the reflectivity is $R \rightarrow 1$, i.e. the ideal case is reached.

Equ. 2.37 shows that a high contrast in refractive index is favorable. Furthermore, the reflectivity becomes higher with an increasing number N of dielectric layers. The resulting increase of the mirror thickness is a disadvantage in optomechanical experiments where low effective mass is needed in order to enhance the coupling. This is one advantage of photonic crystal membranes, which due to their working principle can achieve high reflectivities although they are thin.

3 Pillar Shaped Mechanical Devices

On the road towards structures for optomechanical experiments with Fabry-Pérot cavities that exhibit less dissipation and higher Q-factors, the next step was the further improvement of the cantilevers already used. A major problem was the requirement that the movable mirrors in these experiments had to exhibit excellent optical *and* mechanical properties.

Early devices used in our group were cantilevers cut out of DBR (distributed Bragg reflectors) mirror material (see chapter 2.4.3), Ta_2O_5/SiO_2 . As these first movable reflectors exhibited low Q-factors, the idea was to grow them on a support material with excellent mechanical properties, such as silicon nitride (SiN) (ref. [43]). But the direct contact of the mirror with the mechanical material still decreased the Q-factors to about 3×10^4 at low temperatures (ref. [43]). Another attempt was done with Bragg mirrors made of aluminium gallium arsenic ($AlGaAs$) (ref. [8]), which has not only good optical, but also good mechanical properties. It turned out that these structures were suited as mechanical devices only at room temperature due to unexpected behavior of the Q-factors at low temperatures, that still has to be understood. Therefore, a new direction to be explored is the further separation of the optical and the mechanical component of the movable mirror.

This is exactly the main alteration between the old devices and the new structures presented here. Better separation of the mechanical and the optical function of the devices is achieved by introducing an extra Si layer between the SiN layer responsible for the mechanical behavior of the cantilever and the DBR stack responsible for its optical behavior. In the fabrication process of the devices, the Si layer is etched in such a way that only a thin pillar connecting the disk-shaped mirror to the SiN mechanics is left, which allows for minimal disturbance of the mechanical part by the mirror. These structures are referred to as "pillar structures".

Before starting their fabrication, the planned structures were drawn in Solid-Works and simulated in COMSOL to check the order of magnitude of the resonance frequencies and the mode shapes and improve the design, if necessary. For the fabrication of the devices from the wafer, masks have to be produced that protect certain areas of the wafer during the different steps of the etching process. These masks were drawn in AutoCAD.

Zoom-ins of the AutoCAD drawings of a whole chip with several devices on it and of different designs realizing the pillar-idea are shown in fig. 3.3a-3.3d. On

3 Pillar Shaped Mechanical Devices

each device, a disk-shaped mirror (green layer) with a diameter of 30, 40 or 50 μm is placed on top of a Si pillar. The shape of the underlying mechanical SiN resonator varies between the devices (blue layer). There are beam-shaped devices of different widths and lengths clamped at their ends (see fig. 3.3a, 3.3b), and there are disk-shaped devices held by four or eight auxiliary beams (see fig. 3.3d). Finally, the idea of the pillar is combined with the free-free beam structure described in 2.3.4 (see fig. 3.3c). In these devices, the SiN resonator is shaped like a beam and clamped by four auxiliary beams at different positions along its long edges. Compared to the devices in 2.3.4, the mirror additionally sits on a Si pillar.

Once the devices are fabricated and experimentally tested, it will turn out if the pillar-idea brings an improvement of the mechanical quality factor.

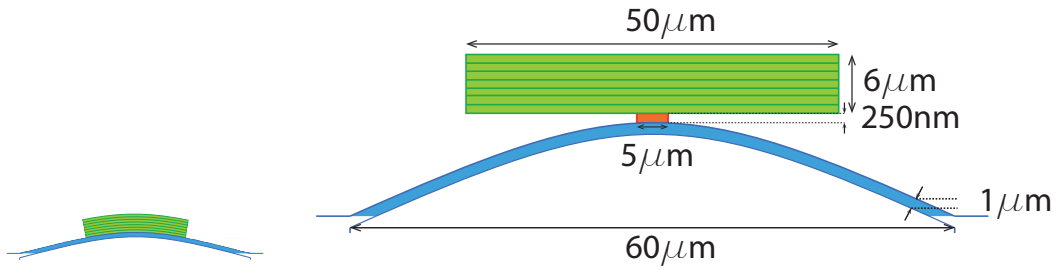
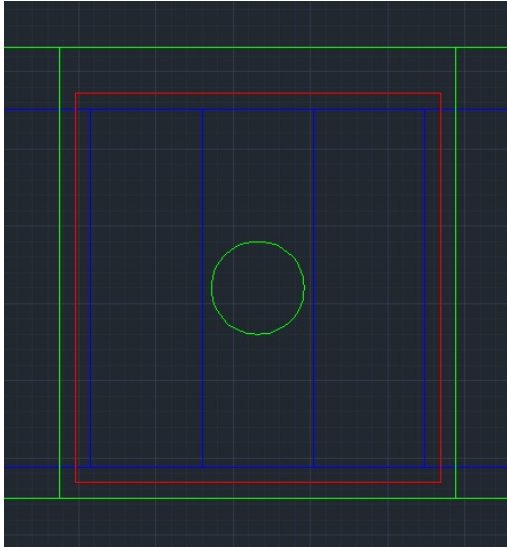
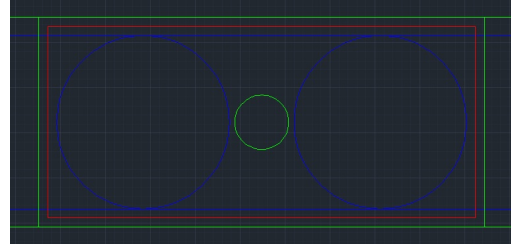


FIGURE 3.1: In the previous structures without the pillar the mirror bends with the mechanical part, which decreases the mechanical quality factor of the device.

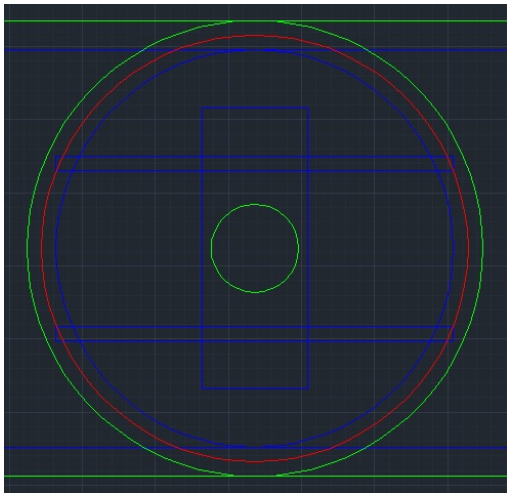
FIGURE 3.2: The additional pillar between the mechanical oscillator and the mirror pad shall prevent the mirror from bending, which helps maintaining the good mechanical quality factor of the device.



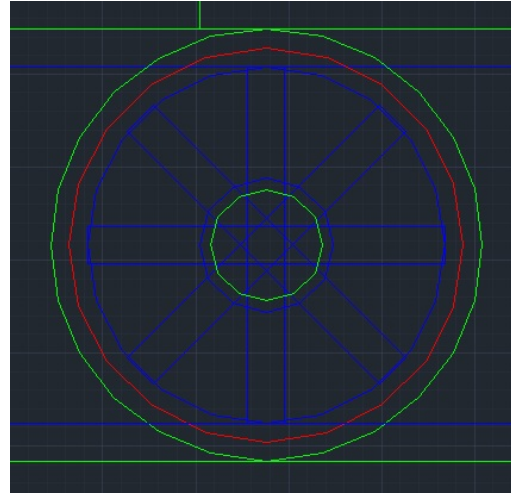
(A) AutoCAD drawing of the layers of a beam-shaped device clamped at its ends. The red layer is for the back-etch, the blue layer for the etching of the SiN layer fulfilling the mechanical function, and the green layer is for the mirror etch. The Si layer between the mirror and the mechanical layer is not explicitly visible as the diameter of the pillar is defined by the back etching time and no extra mask is needed.



(B) AutoCAD drawing of the layers of a beam-shaped device clamped at its ends.



(C) AutoCAD drawing of the layers of a free-free device. The thin auxiliary beams are attached to the long side of the beam.



(D) AutoCAD drawing of the layers of a disk-shaped device held by eight auxiliary beams.

4 Photonic Crystal Membranes

The outstanding potential of photonic crystal membranes is their possible applicability as mechanical elements in the middle of a rigid cavity or even as cavity end mirrors in optomechanical experiments. This requires both, good optical and good mechanical properties. Therefore, important parameters are the optical reflectivity and the mechanical quality factor, Q .

It has already been pointed out that the mechanical properties of optomechanical devices can be enhanced by the separation of the optical and the mechanical function. The "pillar structures" described in chapter 3, are a step in this direction. One can go even further by transferring the mechanical function to membranes, which are mounted in a cavity with two rigid end mirrors. The membranes that are nowadays mostly used in optomechanical experiments are commercial stoichiometric Norcada Silicon Nitride membranes (investigation of their Q -factors for different clampings is described in chapter 5). They are known to give Q -factors up to 10^7 . The idea of photonic crystal SiN membranes is to keep the high mechanical Q -factors observed for SiN membranes despite the holes. In fact, the Q -values of our self-fabricated photonic crystal devices, some beyond 10^6 , are quite satisfactory (see section 4.2).

Another advantage of photonic crystal membranes compared to the previously used DBR mirrors is their smaller effective mass m_{eff} , which leads to higher values for the optical coupling constant $g_0 = \frac{\omega_c}{L} \sqrt{\frac{\hbar}{m_{eff}\omega_m}}$.

This difference in the effective mass of membranes and DBR mirrors is explained by the working principle of the latter (see section 2.4.3). In a DBR mirror, multiple layers of dielectric material are needed for high reflectivities, which implies some micrometers as the minimum thickness of the mirror, while (photonic crystal) membranes consist of only one layer (e.g. Norcada membranes down to 30nm, our photonic crystal membranes 150nm).

With a reflectivity of around 20%, ordinary membranes are good mechanical, but not optical devices. The high reflectivity of photonic crystal membranes is achieved by the holes in the membrane layer which produce the necessary interference effect (see section 2.4, see fig. 4.1).

This means that the idea of photonic crystal membranes is to combine the high Q -factor and the low effective mass of the membranes with the good reflectivity of the DBR mirrors, so that the photonic crystal membranes could be used as movable cavity end mirrors fulfilling both, mechanical and optical requirements.

To find out, if the expected reflectivities can actually be reached, and to learn about the reflectivity behavior of the photonic crystal membranes, we characterized the photonic crystal membranes by reflecting a laser beam off them (see section 4.1).

The mechanical quality factors of the membranes were explored in a fiber interferometer (see section 4.2).

4.1 Optical Characterization of Photonic Crystal Membranes

4.1.1 Photonic Crystal devices

The structures to be investigated were two chips with six working photonic crystal membranes on each. The membranes, made of silicon nitride, are $120 \times 120 \mu\text{m}$ in sidelength, for more details about their dimensions see fig. 4.1. The photonic crystal area has a size of $90 \times 90 \mu\text{m}$, a thickness of 150nm, and is held by four tethers in a hole of $500 \times 500 \mu\text{m}$.

The photonic crystal in the SiN membranes is formed by an array of identical holes. The size of the holes (radius r) and the distance of the holes, a , was varied to get different wavelengths of maximal reflectivity. On one chip (SPJ06c), the size of r and a was swept from membrane to membrane such that the ratio r/a remained constant. On the other chip (SPJ07a), a was held constant, while r and therefore the ratio r/a was swept.

4.1.2 Experimental Setup

An experimental setup for optical reflectivity measurements was built, where a laser beam, which could be tuned in wavelength, perpendicularly hit the membrane. The setup is shown in fig. 4.4.

A fiber-coupled DL pro grating stabilized tuneable single-mode diode laser from Toptica was used as light source. The tuning range went from 985 to 1100nm, with a minimal step size of 0.2nm according to the manufacturer.

The laser light went through tunable fiber polarization controllers (PC) to adjust the polarization that finally exited the fiber. The tuning of the polarization was necessary to branch off some light for the **calibration** at the following polarizing beam splitter (PBS). The calibration curve, taken by detector D2, was used in our first measurements to get rid of the strong laser characteristic (see fig. 4.5). All detectors in this setup were Thorlabs InGaAs Biased detectors with a wavelength range from 700 to 1800nm that covered well the tuning range of the laser. As their detection area is very small, they were put on translation stages for good adjustment.

4.1 Optical Characterization of Photonic Crystal Membranes

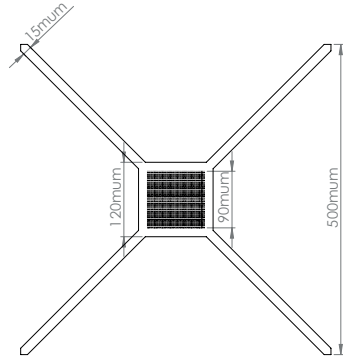


FIGURE 4.1: **Dimensions of photonic crystal membranes.** Their thickness is 150nm.



FIGURE 4.2: **Photonic crystal membrane imaged by a camera.** The camera was placed behind the membrane in transmission. Illuminated by the laser beam (white spot), one can see very well the clamping of the membrane and the photonic crystal area. With the help of the camera, finding the right membrane on the chip and rough beam positioning was fairly easy.

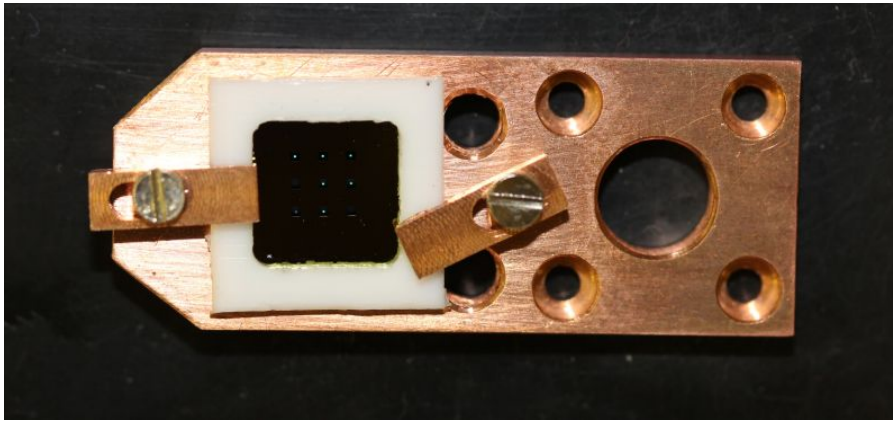


FIGURE 4.3: **Chip with photonic crystal membranes.** The chip is mounted in a copper holder with a teflon frame.

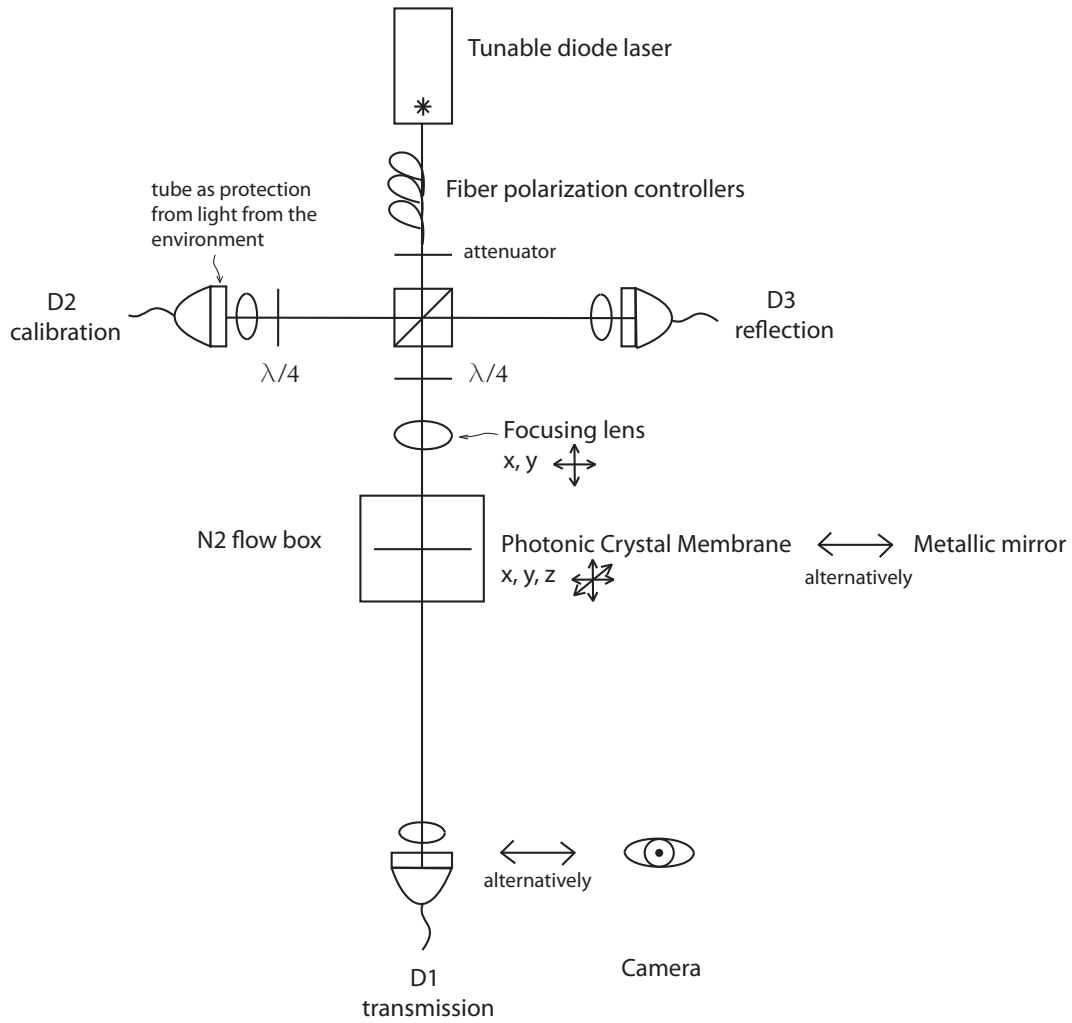


FIGURE 4.4: **Photonic crystal reflectivity setup.** The light emitted by a wavelength tunable diode laser ($985 - 1100\text{nm}$) is split into the calibration beam going to detector D1 and the beam hitting the membrane. The focusing lens in front of the membrane is the crucial lens defining the beam waist at the photonic crystal membrane, which has a great influence on its reflectivity. The light transmitted by the membrane is caught by detector D1, the reflected light by detector D3. This is possible because the horizontally polarized light after the PBS is changed to σ^+ polarization by the $\lambda/4$ waveplate on its way to the membrane, at the membrane it is reflected to σ^- polarization, and finally changed to vertical polarization when again passing the $\lambda/4$ waveplate, such that it is reflected at the polarizing beam splitter (PBS) on its way back. For the positioning of the laser beam on the membrane, detector D1 was substituted by a camera. The mirror was used instead of the membrane in the measurements needed for normalization (see text).

Right in front of the calibration detector D2, a $\lambda/4$ waveplate was mounted, because otherwise reflected light from the calibration arm was transmitted through the PBS to the opposite side to detector D3, causing an offset in the reflectivity measurements. Moreover, black tubes were screwed on all the detectors, in order to shield them from light from the environment.

The light transmitted through the PBS (1 – 3mW@1064nm) went through the focusing lens in front of the membrane, and finally hit the photonic crystal membrane. The function of the focusing lens is to focus the beam coming from the laser such that its waist has the right size yielding maximal reflection of the membrane. The lens is mounted on an x, y translation stage in order to be able to adjust the incident angle of the beam on the membrane (see section 4.1.3.1).

Readout of the transmittivity and reflectivity of the membrane was done by detector D1 and detector D3, respectively. For the **transmittivity**, the transmitted light was directly caught. For the **reflectivity**, a $\lambda/4$ waveplate was put after the PBS to enable the readout. Like that, the light initially transmitted through the PBS is horizontally polarized. Then, the $\lambda/4$ waveplate causes σ^+ circular polarization of the light. Reflection at the membrane led to σ^- polarization of the light on its way back. The second crossing of the $\lambda/4$ waveplate resulted in vertically polarized light, which was reflected at the PBS and could therefore be observed by detector D3.

For the wavelength sweep measurements, an attenuator was placed after the fiber output as otherwise the detectors were saturated.

The chip with the membranes was mounted on translation stages, which allowed for adjustment in x, y, z direction. This was necessary for the positioning of the laser on the membrane.

During the first set of measurements, the membrane was exposed to air. After cleaning the device, for the second set of measurements, a nitrogen flow box was built around the membrane. This was a plexi glass box mounted as a housing around the membrane, with two holes for the laser beam and the nitrogen flow. The nitrogen surrounding the membrane avoided new contamination.

4.1.3 Alignment Procedure

4.1.3.1 Preparation measurements

As those membranes were completely new structures and their properties were still unexplored, some parameters had to be tested before the actual measurements could be done. We investigated e.g., how the incident angle of the laser beam influenced the results, if the reflectivity of the membrane depended on the polarization of the incident beam, if the membrane should ideally be positioned in the beam waist w_0 , and what the ideal size of the beam waist was.

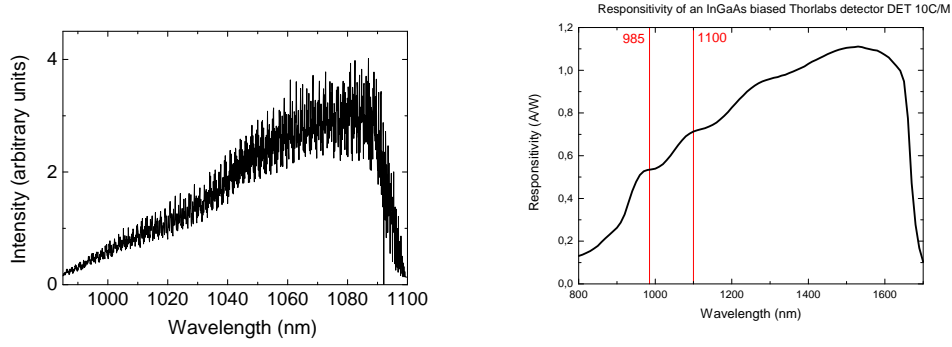


FIGURE 4.5: Laser and photodiode characteristic. The figure on the left-hand side shows the light intensity measured by a photodiode placed directly at the output of the fiber after the laser, therefore it contains the laser and the photodiode characteristic. The figure on the right-hand side shows the characteristic of the InGaAs biased photodiode according to thorlabs. One can see that the intensity variation resulting from the photodiode is only about 25%, which implies that the variation of 300% in the left figure can be ascribed mainly to the variation of the output power of the laser itself. In addition to the strong variation of the output power, the laser exhibits oscillations of high amplitude and high frequency when scanning the wavelength.

Tilt In principle, the light has to strike the membrane perpendicularly. This is explained by the fact that at the interface between two media with different refractive indices (in our case air and SiN), there is a difference in reflectivity and transmittivity between parallel and perpendicularly polarized incident light. This distinction can be avoided by sending the light orthogonally at the boundary. Nevertheless, in some measurements at the beginning, the beam was slightly tilted, which led to a polarization dependence of the transmittivity. We tested the polarization dependence by rotating a $\lambda/4$ or a $\lambda/2$ waveplate in front of the membrane. Graph 4.6 depicts the variation of the transmitted intensity depending on the rotation of a $\lambda/4$ and a $\lambda/2$ waveplate, respectively i.e. depending on the incoming polarization. The periodicity of the transmittivity (four maxima/minima in a 360° rotation) is a result of the periodicity of the waveplates. The third curve on the graph shows the transmittivity for an orthogonally incident beam. There, the transmitted intensity is equal for all light polarizations behind the $\lambda/4$ waveplate. Apart from emphasizing the importance of orthogonal incidence of the beam, this measurement confirmed our assumption that for the measurements in reflection we could place the $\lambda/4$ waveplate in the beam without affecting the results as the reflectivity does not depend on the incoming polarization in the case of no tilt.

Position in beam The next question was, if the maximum reflectivity could actually be achieved with the membrane positioned in the waist ω_0 of the beam, and how strongly the reflectivity deviated when the membrane was not accurately positioned in the focus. The calculations shown in fig. 4.10 and 4.11 were done for plane incident waves, i.e. the membrane placed in the beam waist.

At the fixed wavelength of 1075nm, the reflectivity of the membrane with $a = 932$, $r/a = 40$ was measured for different positions of the membrane in the beam. The wavelength of 1075nm was chosen, as it was in the region of wavelengths yielding the highest reflectivity. This measurement was carried out for different lenses, which means different waist sizes and opening angles. The results show clearly that for all lenses the optimal reflectivity occurs at the waist (see fig. 4.8).

Size of beam waist In a next step, it was interesting to find out the optimal size of the waist. Therefore, reflectivity measurements with five different focusing lenses ($f = 40, 75, 100, 150, 200\text{mm}$) were performed. The membrane was always positioned in the waist of the laser beam at 1075nm wavelength. The wavelength was chosen due to the same reasons as before.

The results, depicted in fig. 4.9, showed that the lens with $f = 100\text{mm}$ and a corresponding waist of $20\mu\text{m}$ yielded the highest reflectivity. The challenge was to find a waist size that is smaller than the photonic crystal area, as otherwise the fraction outside is automatically lost for the reflectivity. On the other hand, for a beam that is too small, the photonic crystal effect does not work properly any more. Computational calculations show that the TEM00 mode of a beam with $20\mu\text{m}$ waist size overlaps more than 99.99% with the $90 \times 90\mu\text{m}$ photonic crystal area.

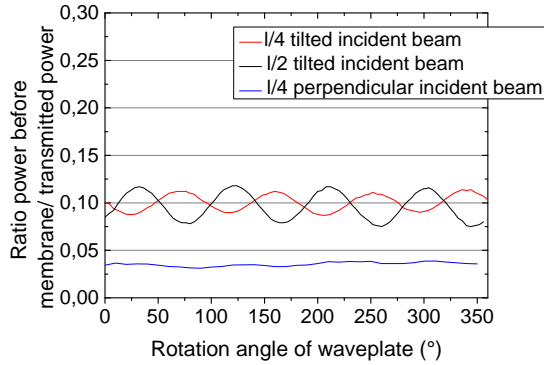


FIGURE 4.6: **Normalized polarization dependence of transmission (power after membrane/power before membrane).** Laser @ 1060nm. Black and red curve: Beam tilted w.r.t. membrane - polarization dependence of transmitted intensity. Blue curve: Beam falls perpendicularly on membrane - almost no polarization dependence.

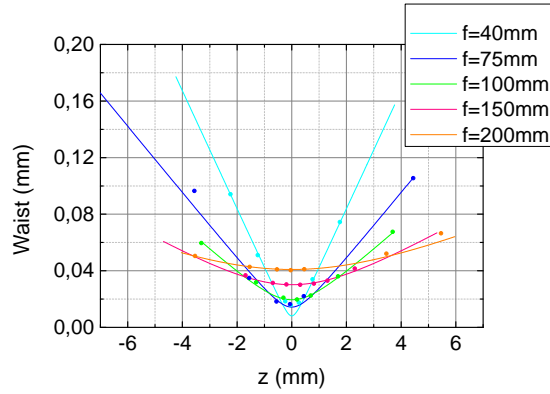


FIGURE 4.7: **Waist size change with z-axis for lenses of different focal lengths.** Curves are a Gaussian beam fit.

Having answered the above questions, it was clear how to set up the actual measurements. From then on, the lens with a waist size of $\omega_0 = 20\mu\text{m}$ was used,

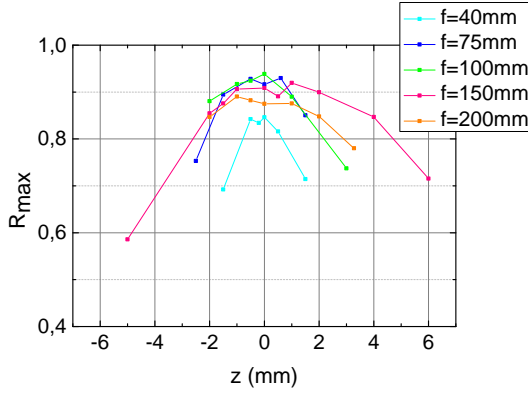


FIGURE 4.8: **Reflected intensity depending on the position of the membrane in the light beam.** Lines serve as a guide for the eye. We used membrane $a = 932\text{nm}$, $r/a = 40$ at a wavelength of 1075nm . Five lenses of different focal lengths were set in as focusing lenses.

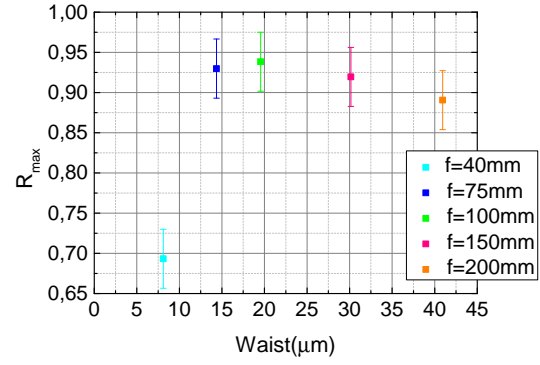


FIGURE 4.9: **Maximum reflectivity.** The maximum reflectivity values of membrane $a = 932\text{nm}$, $r/a = 40$ at 1075nm for the lenses with different focal lengths are depicted. The lens with $f = 100\text{mm}$, corresponding to a waist size of $w_0 = 20\mu\text{m}$, guarantees the highest reflectivity.

the membrane was positioned in the focus of the beam, which hit the membrane perpendicularly.

4.1.3.2 Actual Alignment

Positioning of the membrane in the laser beam The rough positioning of the membrane in the beam could be done easily with the help of a ruler (z position - set membrane in focus of beam) and an ordinary CCD camera (x, y position) with removed infrared filter placed behind the membrane (see fig. 4.4). For the imaging of the membrane, we did not need any extra light source, but used exclusively the laser beam. This was sufficient because the laser beam illuminated the membrane well enough to allow for an unambiguous camera picture (see fig. 4.2). In order to get a sharp camera picture with an appropriate magnification, it was necessary to calculate the object distance g (between the membrane and the lens in front of the camera) and the image distance b (between lens and camera) via the lens equation

$$\frac{1}{f} = \frac{1}{g} + \frac{1}{b}, \quad (4.1)$$

$$A = \frac{b}{g}, \quad (4.2)$$

with the focal length f of the lens in front of the camera and the magnification A .

For a lens of $f = 35\text{mm}$ and a magnification of $A = 9$ (the side length of the total membrane hole was $500\mu\text{m}$, the side length of the camera's CCD chip was $5000\mu\text{m}$) we needed $g = 38.9\text{mm}$ and $b = 350\text{mm}$. With the aid of these calculations, it was

quite easy to find the membranes with the laser beam.

For **fine positioning**, a powermeter was placed after the membrane. Carefully, the translation stage, on which the membrane was mounted, was moved in x , y and z direction until the transmitted power - displayed on the powermeter - was at its minimum. This meant that the membrane was struck at the ideal spot.

As a side remark, I want to mention an interesting observation we made at this point. When the membrane was perfectly positioned, there appeared a symmetric light pattern on a detection card in transmission. It looked like a flower consisting of light points. Obviously, this was a result from the photonic crystal interference.

Another issue is the actual adjustment of the beam **tilt**. This was done by overlapping the beam coming back from the membrane and the incident beam by translating the focusing lens in x and y direction.

Order of adjustment steps

1. Place the membrane in the focus of the focusing lens.
2. Camera in transmission: Search for the right membrane.
3. Beam coming back from membrane overlaps with the incident beam, i.e. no tilt (be careful about not losing the membrane - this step has to be done alternating with the previous one).
4. Optimize the x , y and z position of the membrane by moving the membrane on the translation stage with the micrometer screws such that a powermeter in transmission shows minimal power.
5. Adjust the $\lambda/4$ waveplate in front of the membrane such that the reflected intensity at detector D3 is at a maximum.
6. Adjust the detectors D1, D2 and D3.

At that point, the actual measurements can be carried out. We want to distinguish two types of measurements. The first type are the *wavelength sweeps*, where the reflectivity (transmittivity) behavior of the membranes is measured over a certain wavelength range. This way, the wavelength of maximal reflectivity (minimal transmittivity) can be found. As soon as one knows the optimal wavelength, *measurements at a fixed wavelength* can be performed, which allowed for more accurate, normalized reflectivity measurements.

4.1.4 Wavelength dependent optical characterization

4.1.4.1 Measuring and evaluation methods for wavelength dependent optical characterization

Laser settings for wavelength sweeps: The **wavelength range** of the sweeps went from 985 to 1100nm. We started with measurements in transmission because they were simpler, as the light was caught directly after the membrane without passing the $\lambda/4$ waveplate and the PBS another time.

We chose a laser **step size** of 0.5nm, which was appropriate to resolve the minima (and for the reflectivity maxima) of the curves. This step size was estimated by having a look at theoretical calculations (see fig. 4.10 and 4.11). The designed full-width-at-half-maximum (FWHM) was about 3nm, this justified the step size of 0.5nm.

Calibrated measurements At the beginning of the project, we divided the reflection and transmission curves (detected by detector D3 and D1, respectively) by the calibration curve (detected by detector D2), since we thought, this might eliminate not only the rough laser characteristic (the broad feature), but also the disturbing spikes. This worked to a certain extent, but not as well as we had hoped. But still, the calibrated curves were suited to determine the wavelength of maximal reflectivity (minimal transmittivity) (see fig. 4.13 and 4.14), but could not be consulted for any statements about the percentage of reflectivity, which was essential for the question if the photonic crystal membranes could be used as end mirrors of cavities for optomechanical experiments. Therefore, we soon moved on to normalized measurements.

Normalized measurements To get all the data that is needed for normalized transmittivity and reflectivity measurements, several sweeps were necessary. Therefore, the disadvantage compared to calibrated measurements was that the laser oscillations were eliminated to a lower extent. This was due to the lack of mechanical repeatability of the laser steps, i.e. the wavelength steps of the laser are not perfectly equal in each run. In the calibrated measurements, only one sweep was performed, that is why the spikes on the calibration curve were similar to those on the transmission curve. So the division eliminated them quite well, while this was not the case any more for the normalized measurements consisting of more than one run.

For the **normalized transmittivity**, we first measured in transmission. In a second step, we removed the membrane and recorded the transmission without membrane, i.e. the incident light. Dividing the transmission curves with membrane by the transmission curves without membrane directly gave normalized values for the transmittivity.

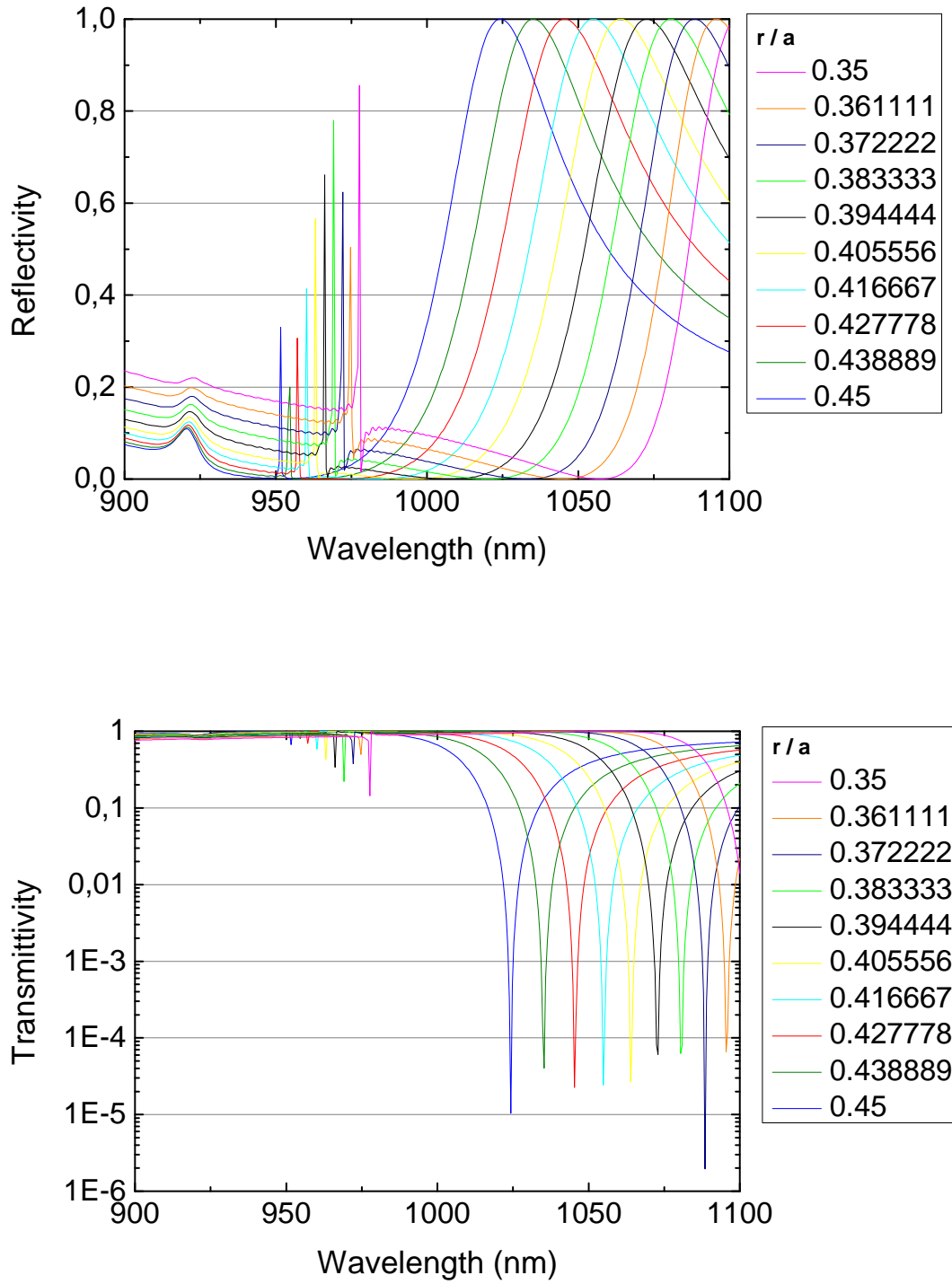


FIGURE 4.10: **Simulated reflection and transmission** of photonic crystal membranes. The distance between the holes is constantly held at $a = 932\text{nm}$, while the radius is swept such that r/a goes from 35 to 45.

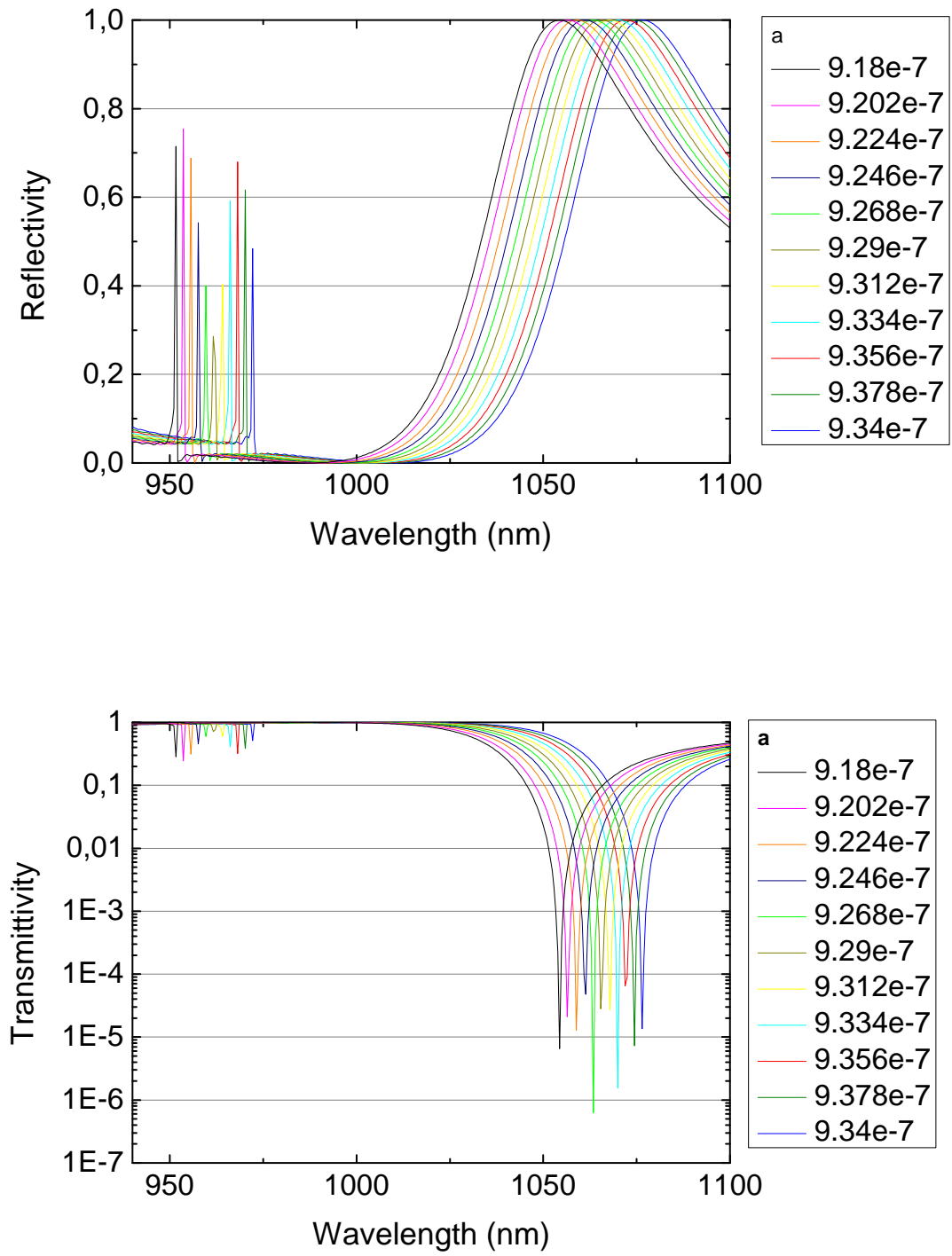


FIGURE 4.11: **Simulated reflection and transmission** of photonic crystal membranes. The radius, r , and the distance between the holes, a , are swept. The value of a ranges from 918 to 940nm. Their ratio remains unchanged at $r/a = 40$.

For the **normalized reflectivity**, a "mirror method" was used. A silver mirror was positioned in place of the membrane and the intensity reflected by the mirror was measured by detector D3. The idea was to calculate the ratio between the membrane reflection curve and the mirror reflection curve. Doing this, one has to take into account that the mirror does not reflect 100%, but that its reflectivity is lower and depends on the incident wavelength. So the mirror had to be calibrated as well before its reflectivity could serve as a reference.

Of course, due to the spikes from the laser characteristic, no precise values for the maximal reflectivity could be deduced by using that method, but it was appropriate as a start. A good cross-check was the summation of these normalized R and T measurements (see fig. 4.12). The outgoing values oscillate around 1. This on the one hand shows that in total the measurement method is reliable, as reflection and transmission are complementary and add up to 1. On the other hand, it becomes again clear that the oscillations of the laser gravely disturb the measurements and preclude precise statements about reflectivity and transmittivity.

Close to 985 and 1100nm, the intensity emitted by the laser varies so strongly between the single sweeps, that after normalization not only the high-frequency oscillations remain but not even the coarse form of the laser characteristic can be compensated and the sum of R and T differs from 1.

4.1.4.2 Results of wavelength dependent optical characterization

Figures 4.13, 4.14 and 4.16 show the measurement outcomes of the wavelength sweeps.

When comparing the reflectivity and transmittivity results of the two different chips (see fig. 4.14 and 4.13), one can immediately see that - as expected from fig. 4.10 and 4.11 - varying the ratio between the hole radius, r , and the hole distance, a , affects the maximal reflectivity (minimal transmittivity) wavelength much more than varying r and a by the same factor, such that the ratio stays the same.

After some measurements, the samples were cleaned with oxygen plasma etching. It was interesting to find out if the exposure of the membranes to air leads to contamination or if oxygen plasma etching effects the reflectivity of the membranes. Comparison of the graphs in fig. 4.14 and 4.16 roughly shows that the cleaning did not change the order of the membranes concerning the wavelength of maximal reflectivity. The graphs in fig. (4.17) clearly demonstrate the tendency of a shift of the wavelength of maximal reflectivity to lower wavelengths. This can be explained by the fact that the holes become bigger when removing the contamination, i.e. the radius r increases together with the ratio r/a , which entails lower wavelengths of highest reflectivity. Again, this matches the simulations (see fig. 4.10 and 4.11).

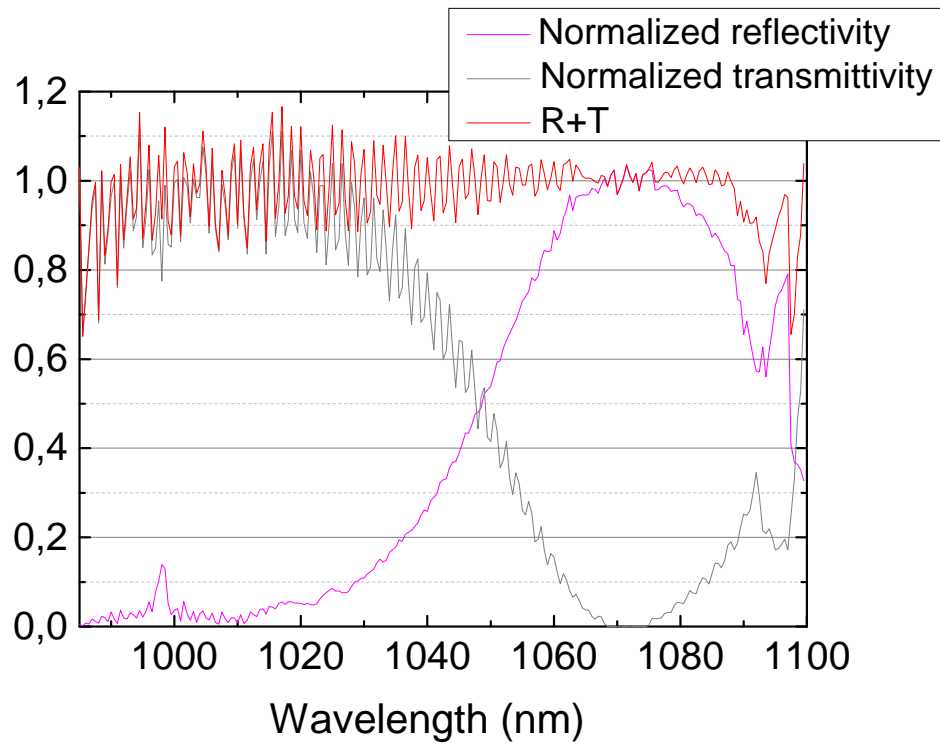


FIGURE 4.12: **Reflection+transmission.** For membrane 9, the pair of reflection and transmission from one sweep is shown, as well as the sum of both, which is oscillating around 1.

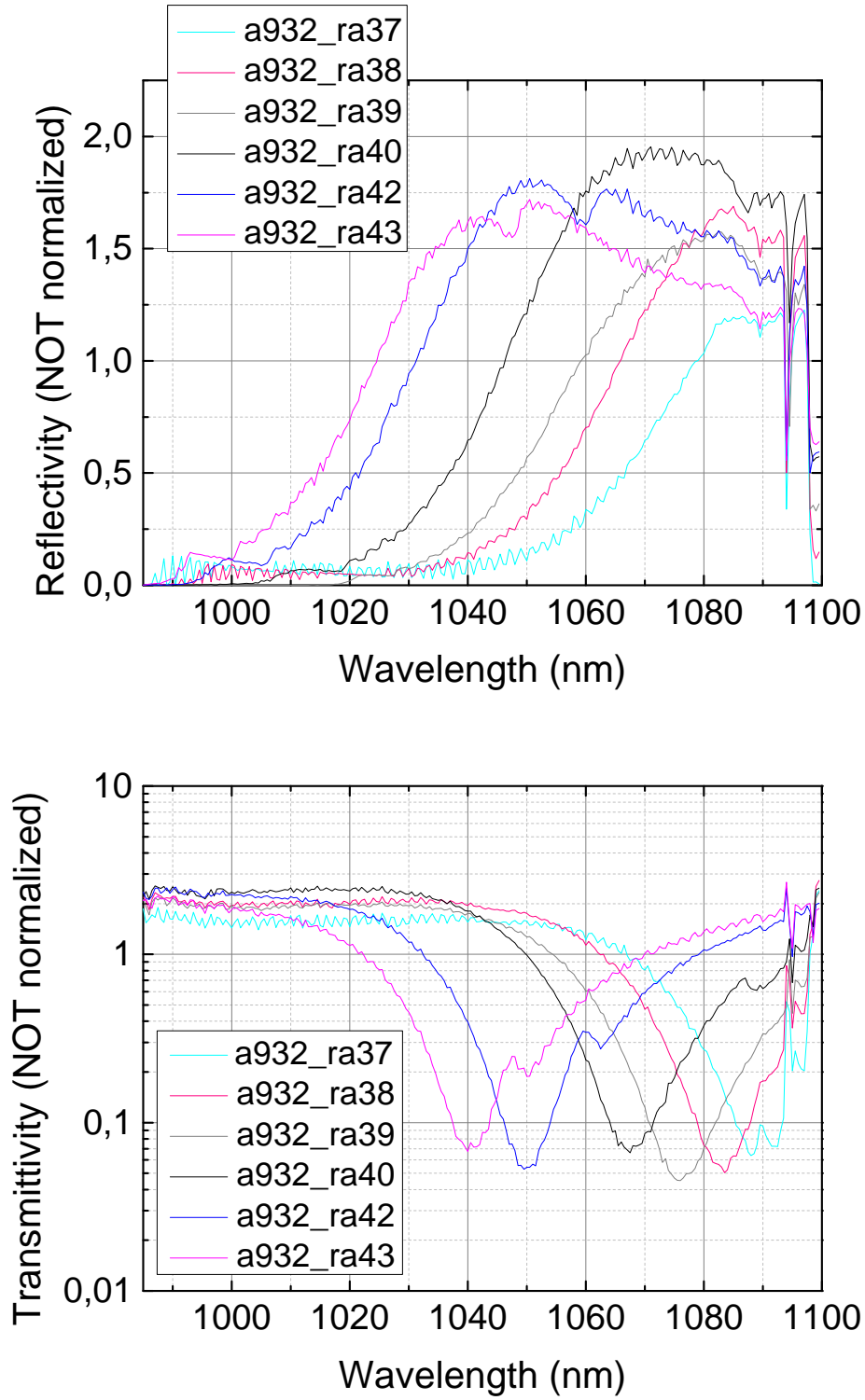


FIGURE 4.13: **Reflectivity and transmittivity of membranes on chip SPJ07a, un-cleaned.** The results are not normalized. It is obvious that altering the ratio between the radius, r , and the distance between the holes, a , results in a significant change of the wavelength of highest reflectivity.

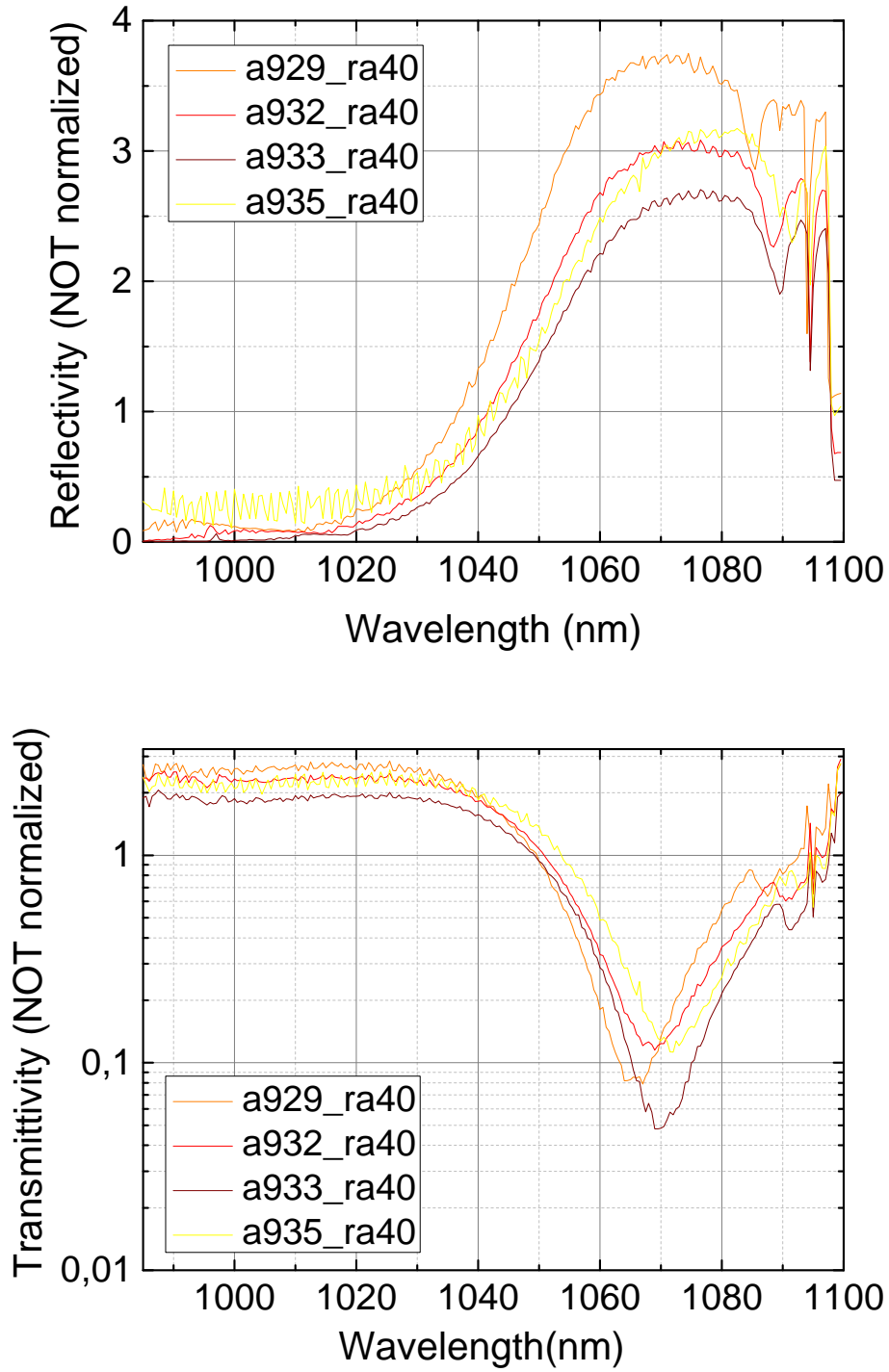


FIGURE 4.14: **Reflectivity and transmittivity of four membranes on chip SPJ06c, uncleaned.** The results are not normalized. The measurements were taken before the cleaning of the chip by oxygen plasma etching. Variation of r and a by the same factor, i.e. leaving their ratio constant, barely leads to a shift of the wavelength of maximum reflectivity.

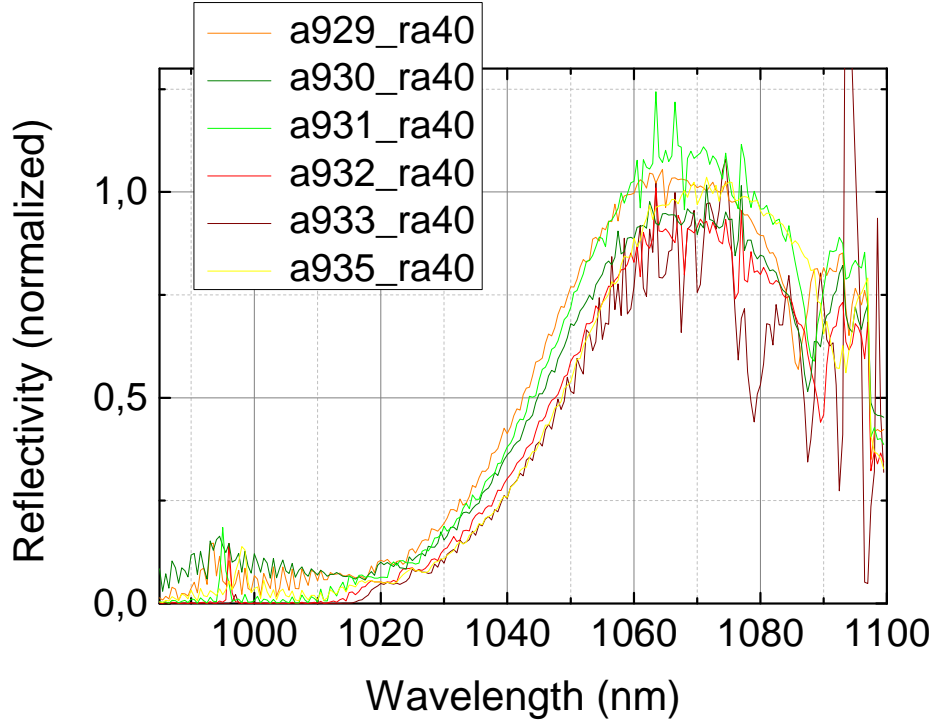


FIGURE 4.15: **Reflectivity of membranes on chip SPJ06c, cleaned.** These are the normalized reflectivity results of all the membranes on chip SPJ06c after it has been cleaned by oxygen plasma etching. The conspicuous spikes on top of the reflection curve remained despite normalization, as in the course of normalization measurements the fine laser characteristic cannot be eliminated because normalization requires more than one measurement but the laser steps are not perfectly repeatable.

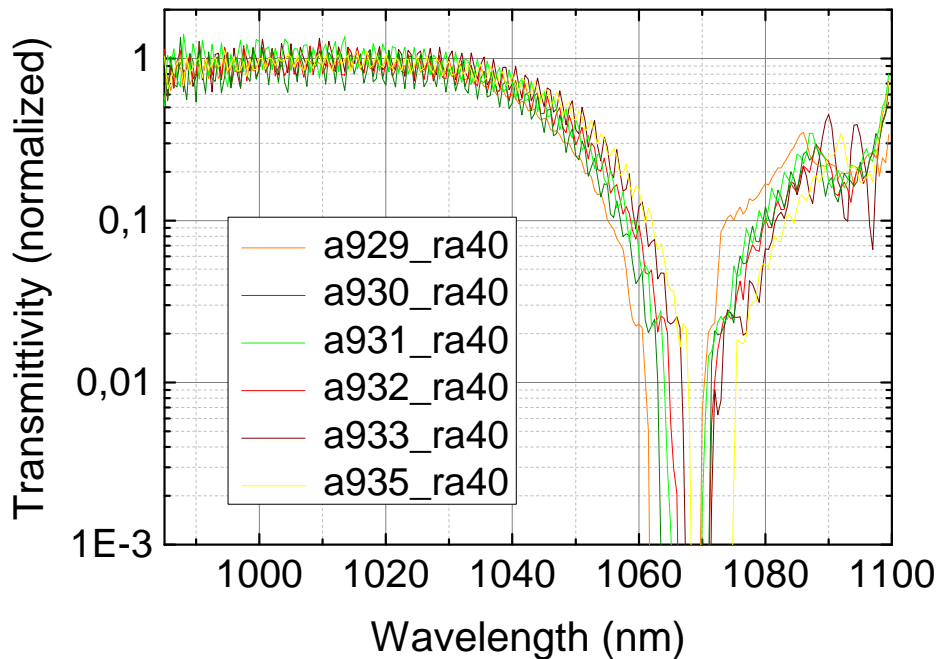


FIGURE 4.16: **Transmittivity of membranes on chip SPJ06c, cleaned.** These are the normalized transmittivity results of all the membranes on chip SPJ06c after it has been cleaned by oxygen plasma etching.

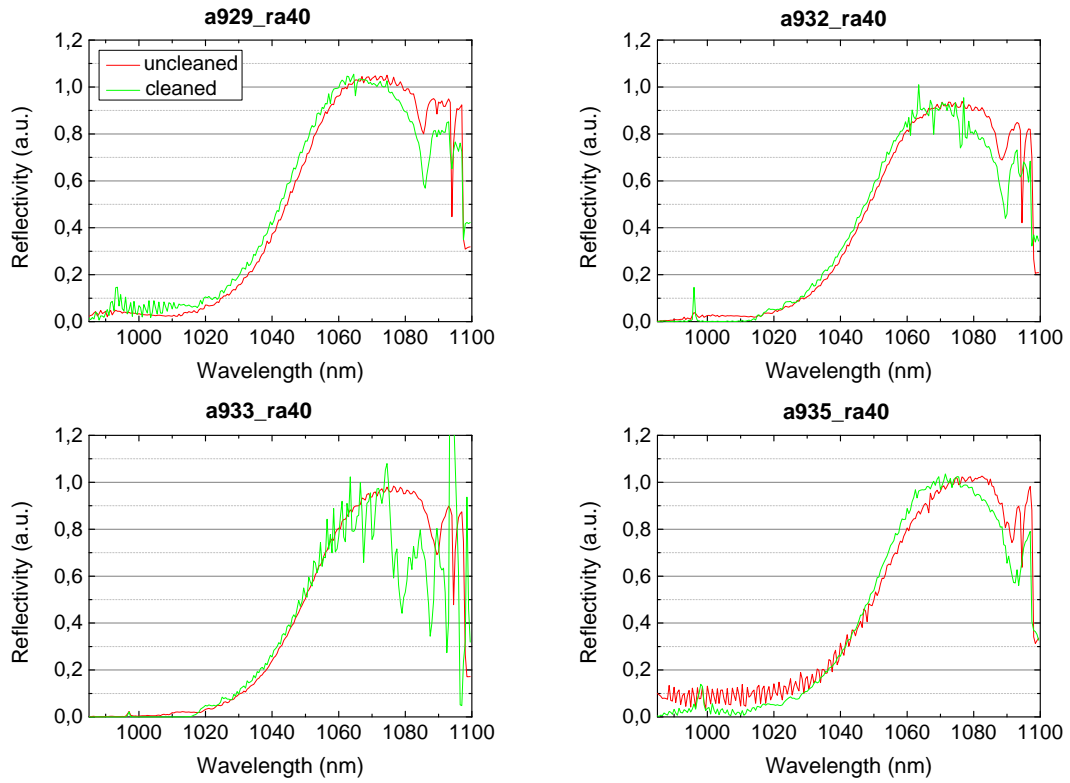


FIGURE 4.17: Comparison of the reflectivity of four membranes on chip SPJ06c in uncleaned (red) and cleaned (green) state. A slight shift in wavelength can be observed. The fall-off in the cleaned curve of membrane *a933,ra40* originates from an accident in which the beam was interrupted for some seconds. The height of the curves cannot be compared, because they were both taken in arbitrary units and then scaled to 1.

4.1.5 Normalized measurements at a fixed wavelength

The **alignment** was the same as for the sweeps, but without the last step of positioning the detectors.

4.1.5.1 Measuring and evaluation methods for normalized measurements at a fixed wavelength

The **measurements at a fixed wavelength** yielded normalized results by applying two different measurement methods.

The first was measuring the incident power directly before the membrane and the reflected power in front of D3 with a powermeter. We are going to refer to this as **direct method**. A problematic point here was the fact, that the losses at the optical components on the way from the membrane to the position of detector D3 had to be taken into account, which represented a significant error source.

To avoid this uncertainty, we employed the above described **mirror method** as the second measurement method. There, the powermeter was mounted in front of detector D3 and remained there for both the membrane and the mirror reflectivity measurement. Since the two measurement outcomes were directly compared, it was not necessary to take into consideration the losses at the optical components in the return path.

4.1.5.2 Results of measurements at a normalized fixed wavelength

Fig. 4.18 shows the normalized reflectivity before and after cleaning for the six membranes on chip 06c. The wavelength on the abscisse was the wavelength of minimal transmittivity in the sweeps of the dirty membranes. The measurements were performed with the direct method. One can deduce a significant improvement of reflectivity after the cleaning for almost all the membranes.

Comparison of the direct method and the mirror method shows that the normalized reflectivities taken by the direct method are somehow higher than those of the mirror method, as indicated in graph 4.19. However, within the error bars, the results of the two methods are in good agreement. Furthermore, due to the error bars all reflectivity measurements touch the realistic region of reflectivities under 1.

The fairly big errors of several per cent reflect the fact that these measurement methods are not suited for precise reflectivity measurements. As described before, the results rely on measurements with a powermeter. The errors mainly arise due to the highly inhomogeneous detection area of the powermeter. The measured power depends to a high extent on the position, at which the beam falls on the detection area. The errors of the direct method are higher, because more measurement steps were involved due to the correction of the losses at the optical components.

The exact values of the shown error bars are obtained by using a power of around $P = 2\text{mW}$, and an uncertainty of approximately $\Delta P = 0.03\text{mW}$.

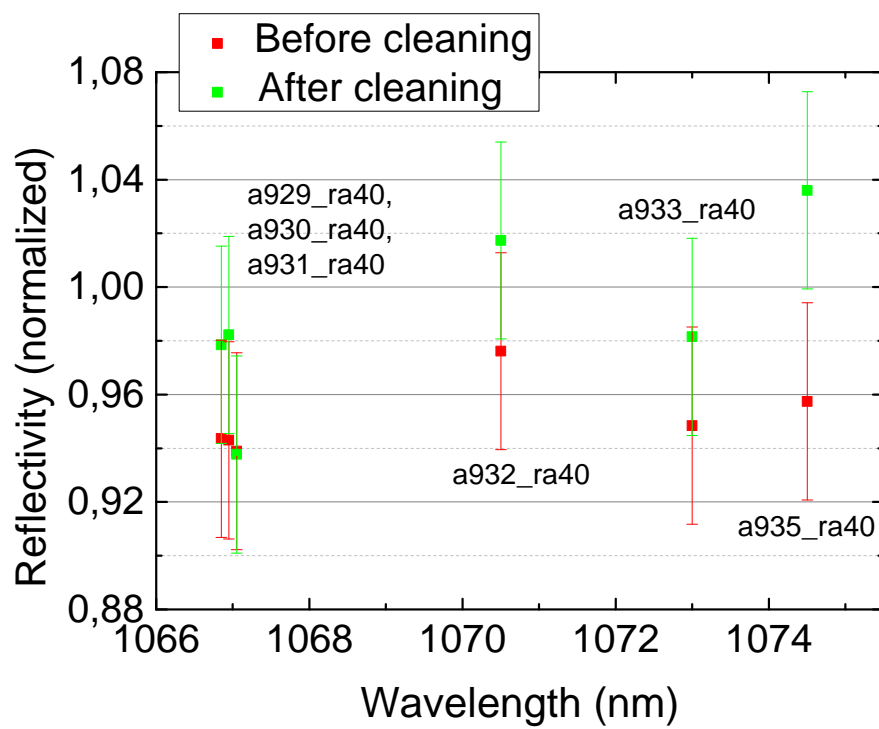


FIGURE 4.18: **Comparison of normalized reflectivity of cleaned and uncleaned membranes** on chip SPJ06c @ wavelength of maximum reflectivity before cleaning. Reflectivities beyond 1 sometimes occur because of the big uncertainty in the measurements.

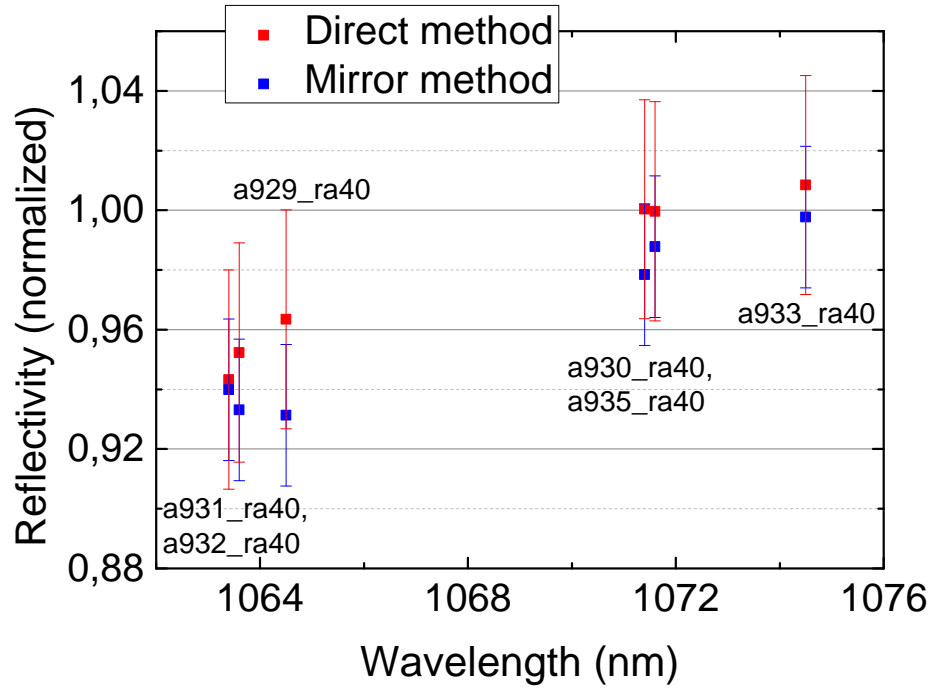


FIGURE 4.19: **Comparison of direct and mirror method** for measuring the normalized reflectivity of the six membranes on chip SPJ06c @ wavelength of maximum reflectivity after cleaning.

Altogether, the results of the normalized reflectivities look very promising. After the cleaning, most of the membranes exhibit reflectivities beyond 98%, which means that it might actually be possible to use the membranes as cavity end mirrors. But due to the high errors of the measurements method of simply hitting the membrane instead of using a cavity, no clear statement can be made. In order to obtain precise results for the maximum reflectivity, a cavity has to be built.

4.2 Mechanical Characterization of Photonic Crystal Membranes

After the optical properties, the mechanical properties of the photonic crystal membranes were investigated. Due to high quality factors for other SiN membranes (see e.g. ref. [32]), the expectation was that the photonic crystal membranes exhibited Q-factors beyond 10^6 . However, this was not clear as they could be decreased in the course of the microfabrication process.

4.2.1 Experimental setup

For the measurements of the Q-factor, a fiber interferometer (for a description, see also ref. [28]) was used.

The fiber interferometer is sketched in fig. 4.20. A Nd:YAG laser at a wavelength of 1064nm was used as light source. In the whole setup, the light is guided in single mode fibers. Only directly in front of the photodetectors at the end, the light exits the fibers and is focused on the photo diode detection area with a lens.

The **signal** beam is the light exiting one output of the variable ratio coupler 1 (VRC1), i.e. a beam splitter enabling a variable splitting ratio, right after the laser. The light from this channel goes to the membrane in the chamber, experiences a phase shift there, and is finally read out in the homodyne detection. In the signal path, the two fiber polarization controllers (FPC) and the fiber polarizing beam splitter (PBS) are the fiber analogue of the composition of fiber polarization controllers, polarizing beam splitter (PBS) and $\lambda/4$ waveplate in the reflectivity setup (see 4.4) - they enable the detection of reflected light. FPC1 are adjusted such that as much light as possible goes through the fiber PBS ("horizontal polarization"), by FPC2 the polarization of the light is changed to σ^+ , at the membrane to σ^- , and eventually to vertical polarization when again passing FPC2. Hence, the back-traveling light is reflected at PBS1, before being combined with the local oscillator (LO, see next paragraph) at VRC2. For the homodyne read-out, the difference signal of the two detectors was obtained with a low loss power combiner/splitter and displayed on a spectrum analyzer.

To enable homodyne detection, apart from the signal beam, a **local oscillator (LO)** beam is needed as a reference beam. This function is fulfilled by the light ex-

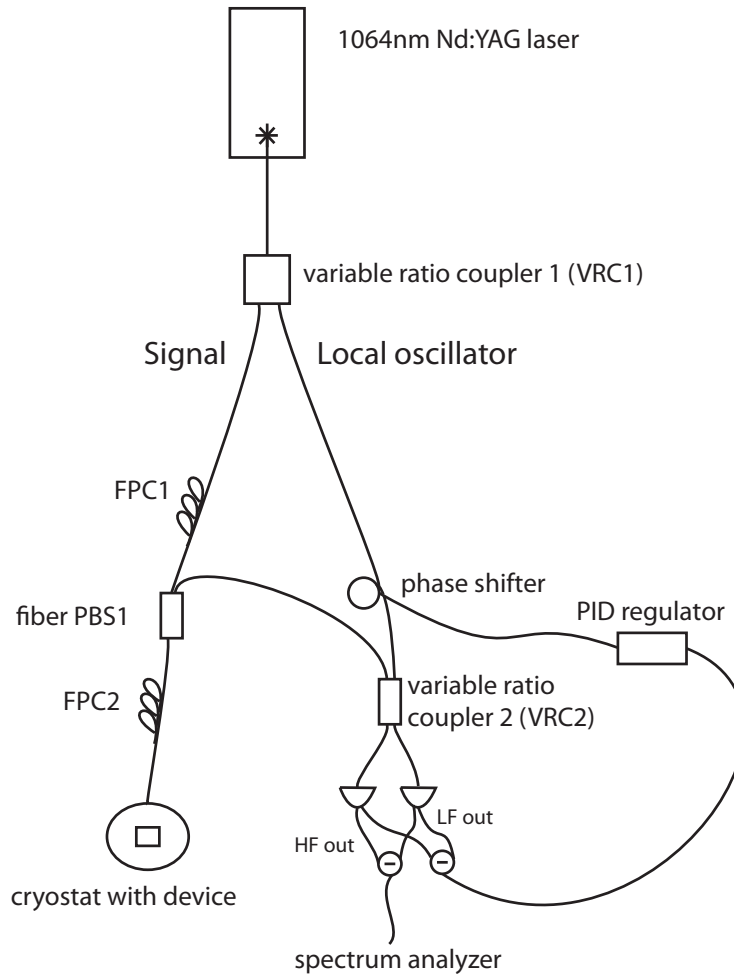


FIGURE 4.20: **Setup of fiber interferometer for Q measurements.** Similar to a Mach-Zehnder interferometer, the laser beam is split by a beam splitter with adjustable splitting ratio, called variable ratio coupler 1 (VRC1), into two separate beams, the local oscillator (LO) and the signal. The position shift from the oscillation of the membrane causes a phase shift on the signal beam in the experimental chamber, before it is recombined with its phase reference, the LO, by another variable ratio coupler (VRC2). From the high frequency (HF) difference signal of the two photodiodes, the resonance frequencies and the quality factor of the membrane can be read out. The low frequency (LF) signal is used to lock the LO to the signal beam such that the detection is maximally sensitive to the phase of the signal beam.

iting the second output of VRC1. The length of the LO is permanently regulated in order to keep the phase between the LO and the signal constant, that means short-time fluctuations and long-term drifts in length, and therefore phase must be compensated. To be able to keep the phase difference, i.e. do the "**locking**", the difference signal of the low frequency (LF) outputs of the photodetectors is fed into a PID-regulator (proportional, integral, differential), which applies a voltage signal to the PZT fiber stretcher in the LO according to the LF difference signal it got. The phase difference that must be held constant by locking is $\pi/2$ for the ringdown measurements, corresponding to maximal detection sensitivity to phase shifts in the signal beam. Best detection of the phase is required because, as mentioned before, exciting a membrane in the cryostat chamber is equal to a position change of the membrane, which imprints a phase shift on the signal beam that is read out in the homodyne detection to find out the mechanical resonance frequencies and the quality factors of the membrane. Balancing of the signal and the LO beam is done electronically with an attenuator after one of the detectors.

In the **cryostat chamber**, the membrane is placed on top of a stack of nanopositioners from attocube. They allow for very precise positioning in x, y and z direction over a centimeter range with an accuracy of a few nm in vacuum at low temperature. Between the membrane and the attocubes, there are additionally a copper plate, a piezoelectric crystal, or a membrane holder. Directly connected to the cold finger via copper braids, the plate should facilitate the thermalization of the membrane chip during measurements at low temperature, which could be performed in the cryostat by using 4He. Measurements at cryogenic temperatures were not carried out for the photonic crystal membranes, but only for the Silicon Nitride Norcada membranes (see Chapter 5). For the Q-measurements of the photonic crystal membranes, the membrane chip was directly placed on the flat piezo, that was screwed on the thermalization plate and the attocubes. The piezo was driven by an external frequency generator.

For all Q-measurements, the chamber was evacuated to a pressure of $10^{-4} - 10^{-5} \text{ mbar}$ with a turbo pump.

4.2.2 Alignment procedure

After we had placed the chip with the membranes in the chamber, we had to find the right membrane and adjust it such that it was struck at the ideal spot, where it reflected as much light as possible. This time, there were three degrees of freedom to be adjusted - the plane in which the membrane was placed (x, y) and the direction perpendicular to it (z).

The first thing to do was to adjust the distance (**z-direction**) between the membrane and the fiber tip, which consisted of a small focusing lens, such that a maximum of the signal was reflected from the membrane back into the fiber. This is

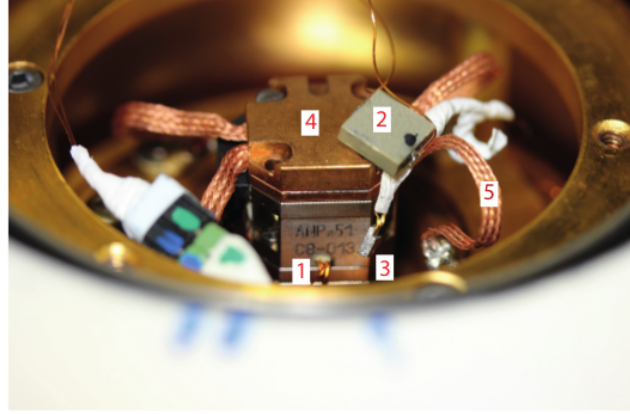


FIGURE 4.21: **A glance into the cryostat.** The stack of the attocubes (1), the piezo-electric crystal (2) (the one we used for the Silicon Nitride Norcada membranes), the temperature sensor (3) (used for measurements at low temperatures), and the thermalization copper plate (4), connected with copper braids (5) to the cold finger, are visible.

equal to stating that the membrane had to be positioned in the focus of the lens. Therefore, the **coarse** height of the fiber was changed manually by moving the fiber end plus the lens up and down in the tube where it was mounted, while checking the reflected power with a powermeter. During this procedure the chamber was open. Then, in the closed chamber, **fine** adjustment with the z-attocube was done, still by looking at the powermeter. This had to be done after pumping out the air of the cryostat, because the entire system contracted during the evacuation. Moreover, the chip sometimes moved in the $x - y$ -plane due to the air drag and the contraction.

The next step was finding the membrane by moving the chip in the **x-y-plane**. From that point on, we changed from the powermeter to the spectrum analyzer to check if the membrane was hit. When the frequency generator, which drove the piezo, generated white noise, there appeared mechanical peaks on the spectrum analyzer as soon as the laser was positioned correctly. In order to find the membrane, the imaging with an optical microscope including a camera, was helpful, but not too reliable, as the picture was distorted due to the angle between the camera and the chip. But if the camera was positioned in the right way w.r.t. the chip, the image was correct in one of the two directions (x/y), so only one degree of freedom was left, and it was possible to operate the remaining attocube until the mechanical peaks appeared on the spectrum analyzer.

4.2.3 Measuring and evaluation methods

Once, the membrane was properly hit and the mechanical resonance frequencies were visible at the spectrum analyzer, everything was prepared for the actual mea-

surements of the Q-factor, the ringdown measurements.

Ringdown measurements As mentioned before, the driving of the membrane in order to get an overview over all its resonance frequencies was done with white noise from a frequency generator applied to the piezo. This showed all mechanical frequencies at the same time. Once having identified the resonance frequencies of the membrane, the Q-factors of the single frequencies could be measured one by one by making ringdown measurements.

A sinusoidal signal with one of the resonance frequencies was applied in the burst mode of the frequency generator. This means that the membrane is excited with a certain frequency a certain number of cycles. Then the signal is shut off, so that the ringdowns can be observed. These bursts are repeated periodically after a given time interval (burst time). In our case, the burst time was 1 second, the number of cycles per burst was 20000.

During the excitation, the amplitude of the membrane goes up to its maximum, and decays exponentially when the driving is turned off. The faster the decay, the lower is the Q-factor.

The drop-off can be analyzed by two different methods. For the first method, traces are taken with an oscilloscope, for the second, with a spectrum analyzer. In both cases, for the evaluation, the exponential energy decay of the damped mechanical mode is drawn on a semi-logarithmic scale, so that it becomes linear with slope $-\gamma_m$, the full-width-at-half-maximum of the energy decay of the mechanical mode m .

$$I = I_0 \exp[-t\gamma_m] = I_0 \exp\left[-\frac{t}{\tau_m}\right] \quad (4.3)$$

$$\ln[I] = I_0 - t\gamma_m \quad (4.4)$$

I_0 : initial energy

τ_m : time after which the energy of the mechanical peak has decayed to $1/e$ of its initial value

Knowing γ_m and the excitation frequency f_m , the Q-factor directly follows by

$$Q = \frac{2\pi \cdot f_m}{\gamma_m}, \quad (4.5)$$

as defined by equ. 2.13.

In the **oscilloscope** method, the ringdown trace $V(t)$ from the oscilloscope shows the amplitude oscillations - they have the period of the driving frequency f_m and an exponentially decaying envelope. These traces were squared to get the energy traces, and converted into a semi-logarithmic scale, as mentioned above, such that

with Mathematica a linear function with slope $-\gamma_m$ could be fitted to the envelope and Q could be calculated.

For the **spectrum analyzer** (SA) method, the ringdown trace was recorded in the zero-span mode of the spectrum analyzer and then evaluated with a Labview program.

The zero-span mode is an operating mode of the spectrum analyzer, in which one frequency and a band width (usually 10kHz in the present experiments) is chosen and continuously monitored. This gives traces showing the intensity of the frequency - in our case the resonance frequency - dependent on time. On the logarithmic dBm scale of the spectrum analyzer, this directly results in linear envelope traces with slope $-\gamma_m$ for the ringdowns (see fig. 4.22).

The formula for the calculation of Q implemented in the program is

$$Q = \frac{2\pi f_m \cdot 10 \cdot \log_{10}[e]}{\alpha}, \quad (4.6)$$

where α is the slope of SA curve, and e is Euler's number.

The slope α corresponds to γ_m with minor modifications since the SA measures in dBm, requiring a transfer from the logarithm with the base of 10 to the natural logarithm.

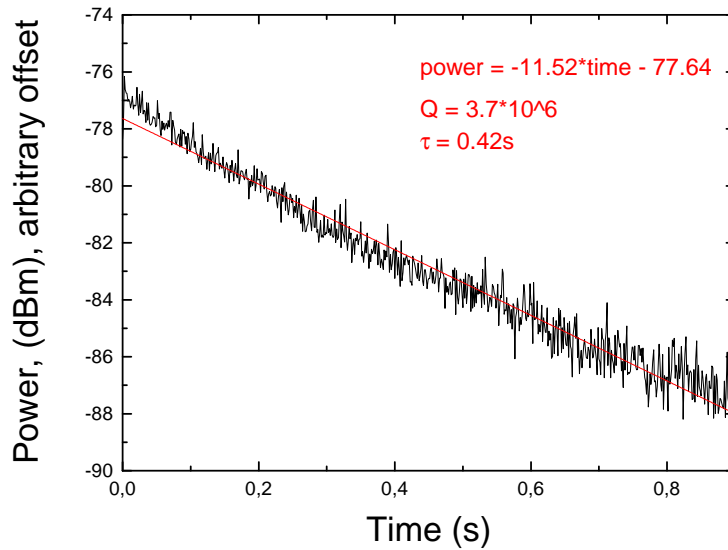


FIGURE 4.22: **Ringdown on the spectrum analyzer.** Membrane 8, round holder, no clamping, RT, 1.59MHz.

The first ringdown measurements were evaluated with the oscilloscope method before changing to the SA. The results of both methods were in excellent agreement.

4.2.4 Results

In fig. 4.23 the results of the ringdown measurements of the photonic crystal membranes are depicted. The Q-factors of the frequencies which could be addressed are shown.

First, we want to find out which modes we measured by comparing with simulations (fig. 4.24a-4.24j). Comparison of fig. 4.23 with the simulations fig. 4.24a-4.24j shows that the fundamental mode of the measured photonic crystal membranes oscillates at a frequency of $f_1 = 359\text{kHz}$. The measured modes with $f_2/f_3 = 808\text{kHz}$ correspond to the calculated mode 2 and 3. Simulated mode 4 could not be measured because the membrane itself was not elongated but only the clamping beams. The measured mode with $f_5 = 1.187\text{MHz}$ corresponds to the 5th calculated mode. Calculated mode 6 to 9 were again not visible. Calculated mode 10 was probably measured at a frequency of 1.405MHz .

The quality factors of all the membranes are higher than 10^5 , which is quite good, some are even beyond 10^6 , which is excellent. The results show that the mechanical quality factors of our SiN photonic crystal membranes can compete with those of commercially fabricated SiN membranes, meaning that it is worth going further in that direction.

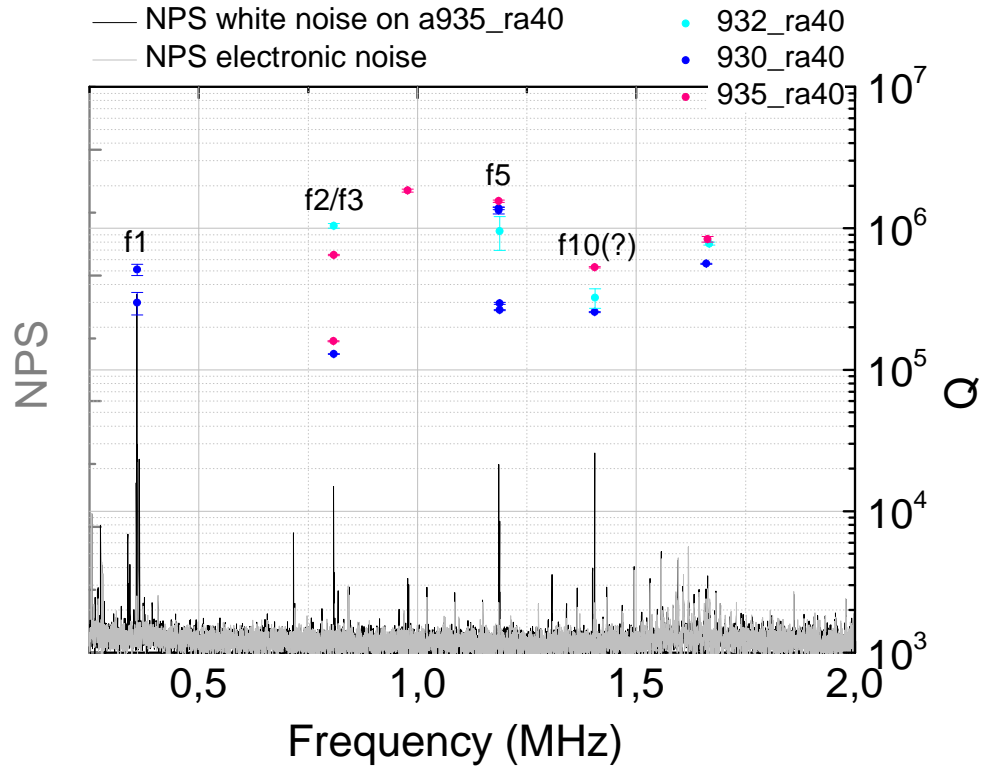
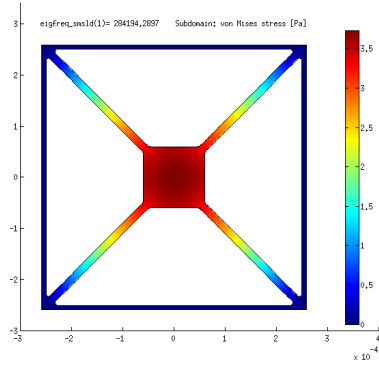


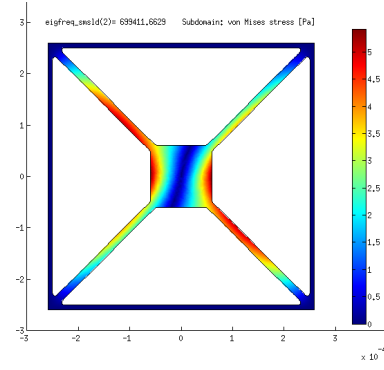
FIGURE 4.23: **Q factors** of the photonic crystal membranes measured at room temperature at a pressure of approximately 10^{-5}mbar .

4.2 Mechanical Characterization of Photonic Crystal Membranes

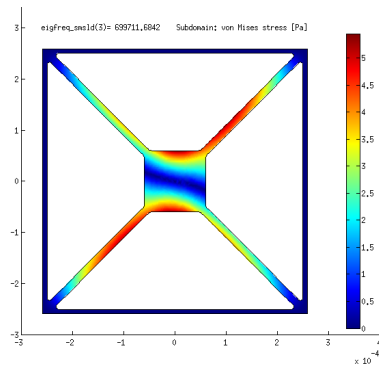


(A) **Simulated mechanical modes of the photonic crystal membranes.**

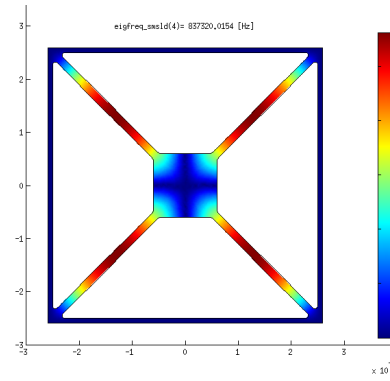
Mode 1, $f_{1theo} = 284\text{kHz}$



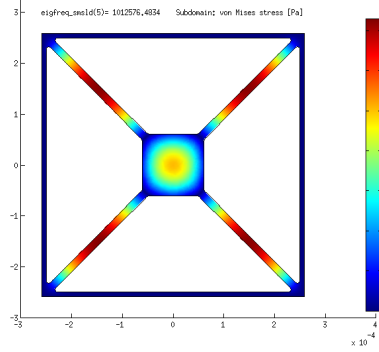
(B) Mode 2, $f_{2theo} = 699\text{kHz}$



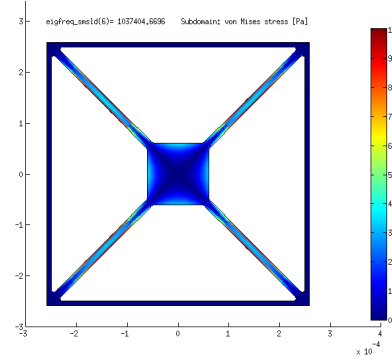
(C) Mode 3, $f_{3theo} = 700\text{kHz}$



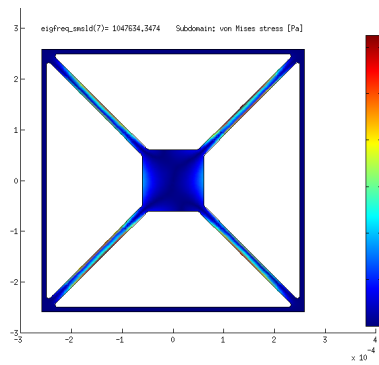
(D) Mode 4, $f_{4theo} = 837\text{kHz}$



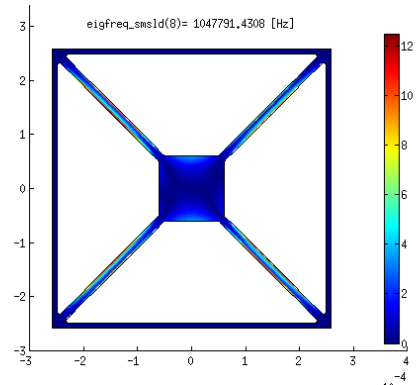
(E) Mode 5, $f_{5theo} = 1.012\text{MHz}$



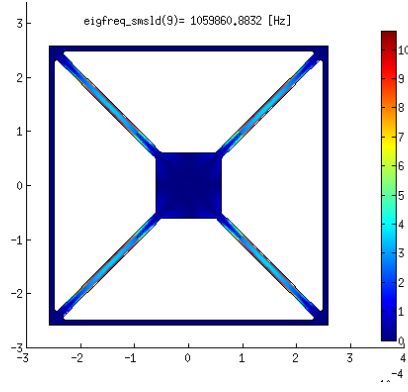
(F) Mode 6, $f_{6theo} = 1.037\text{MHz}$



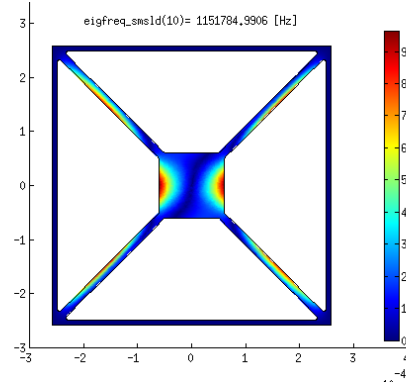
(G) Mode 7, $f_{7theo} = 1.048\text{MHz}$



(H) Mode 8, $f_{8theo} = 1.048\text{MHz}$



(I) Mode 9, $f_{9theo} = 1.060\text{MHz}$



(J) Mode 10, $f_{10theo} = 1.152\text{MHz}$

4.3 Summary

Altogether, the photonic crystal membranes are very promising optomechanical devices which should be further investigated in the future. Their outstanding optical and mechanical properties have been shown.

First, the experiments confirmed that the wavelength dependence of the reflectivity of the photonic crystal membranes matches the simulations. This means that one has good control over defining the wavelength of maximal reflectivity and therefore devices for specific needs can be fabricated.

Furthermore, the measurements show that peak reflectivities approaching 1 can be achieved with the new devices. As depicted in fig. 4.18, there are single membranes, e.g. $a935_r a40$, which have the reflectivities required for using the photonic crystal membranes as cavity end mirrors (see chapter 2.2.1.3).

Future characterization of the optical properties of the photonic crystal membranes should be performed with an optical cavity.

Measurements of the mechanical quality factors of the photonic crystal membranes in a fiber interferometer revealed the membranes' good mechanical properties. The Q-factors for all modes from the fundamental mode of 359kHz up to 2MHz for three membranes were higher than 10^5 , some beyond 10^6 . Further exploration of the mechanical properties is necessary.

5 Quality Factors of Silicon Nitride Membranes

As described in chapter "Photonic Crystal Membranes", membranes were a tool to improve quantum optomechanical experiments. By separating the optical and the mechanical component in the experiments, firstly, the coupling between light and mechanics could be enhanced due to the smaller effective mass, and secondly, outstanding Q-factors could be achieved due to the membranes' excellent mechanical properties.

Membranes with precisely these good quality factors are by now wide spread. The first step when setting up an experiment with those membranes is to reproduce the Q-factors in the separate setup of a fiber interferometer, which is described in this chapter. In order to assure compatibility to our other experiments, different kinds of mounting and clamping of the membrane chip, that could subsequently be used there, were tested in this environment.

5.1 SiN Membranes

The common type of membranes used in optomechanical experiments are Silicon Nitride membranes, provided by the Canadian company Norcada. They have been studied and used by several groups (see ref. [23], [30], [34], [35], [32], [31]) and are known for their extraordinarily high Q factors up to 10^7 .

These membrane chips consist of two layers. A thin Silicon Nitride film, forming the membrane, is deposited on a much thicker Silicon wafer, the frame (see fig. 5.1). They are available in several versions with slightly modified dimensions. For the exact dimensions of the investigated chips, see fig. (2.3).

5.2 Experimental Setup, Alignment, Measuring and Evaluation

For the measurements, the same **experimental setup** as for the Q-measurements of the photonic crystal membranes was used, as well as the **alignment, measuring** and **evaluation** procedure were equal in principle. However, the chip was mounted in a **holder**, that in its final design was compatible with an optical cavity. The

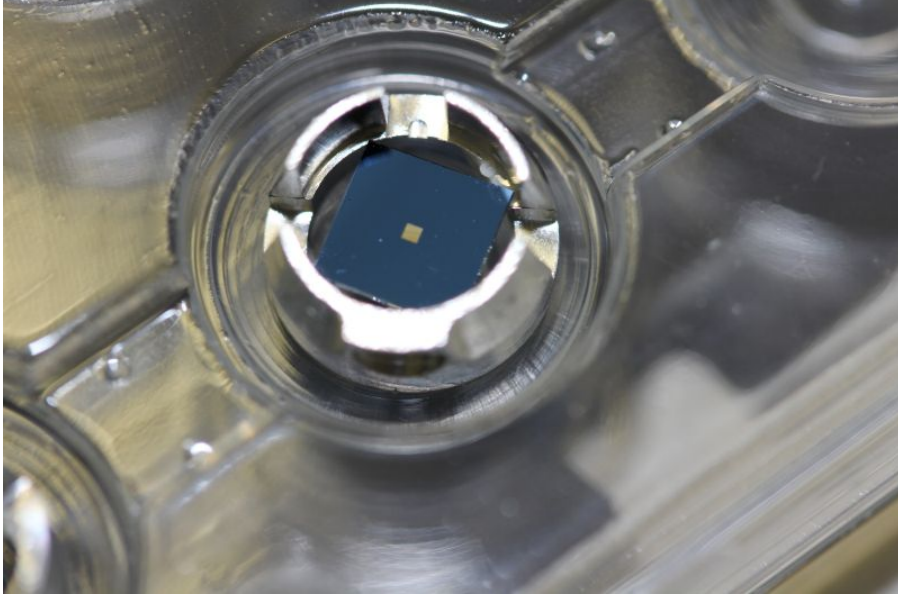


FIGURE 5.1: **Silicon Nitride Norcada chip.**

task was to try out various shapes of holders and test diverse methods of fixing the membranes in the holder to find the one which yielded the highest Q-factors.

A side effect of the usage of a holder was that we could not use the flat piezo from the photonic crystal measurements. The reason was that it was squeezed between the thermalization plate and the holder, and therefore could not move any more. So we switched to another piezo (see fig. 4.21), which was mounted on the holder next to the membrane by screws. This way, the excitation was transferred to the membrane via the holder, while the piezo was not blocked.

After a membrane had been placed in the fiber interferometer, we excited it with white noise from the frequency generator and searched for the fundamental mode. Based on its frequency, we calculated the frequencies of the higher-order modes with $f_{m,n} = \sqrt{\frac{\sigma}{4\rho}[(\frac{m}{l})^2 + (\frac{n}{w})^2]}$, where σ is the tensile stress of the membrane, ρ is the density of the material, m, n is the mode number and l, w are the side lengths of the membrane. The results from this calculation were accurate up to a few kHz, which made it an appropriate means to find and identify all modes of the SiN membranes.

5.2.1 Various holders and clampings

In a first attempt, as a reference, the membrane was **directly**, without a holder, placed on top of the driving piezo on the attocube stack to be as free from any influence as possible. This method resulted in disappointing Q-factors of $10^3 - 10^4$ for the fundamental and the 1,2/2,1 mode. This is contrary to other reported experiments (see ref. [32]), where membrane chips horizontally placed on a holder


FIGURE 5.2: **Round holder.**

FIGURE 5.3: **Square holder.**

without clamping yield the best quality factors. Nevertheless, since it was clear that eventually the membranes had to be positioned in a holder, we decided to focus on that and ignored the bad results from this run.

The requirements of a holder were enabling high Q-factors, the suitability for cryogenic temperatures and the compatibility with an optical cavity, i.e. certain size and material of the holder, and freedom of positioning in the $x - y$ -plane.

Concerning high Q-factors, the method of fixation of the membrane on the holder plays a crucial role. There are two options, namely **gluing** (ref. [25], [34]) and **mechanical clamping**. The advantage of gluing is, that the glue can be put on the Silicon frame side of the chip, so that the membrane itself is not touched. The most important argument for mechanical clamping is the fact that the membranes can be easily exchanged. This entailed benefits, for example several membranes could be tested in the same holder to find out the deviation of the Q-factors between the membranes themselves. Furthermore, one membrane could be investigated in different holders, which was needed to find out a good holder design. Thus, we started the investigation of proper mounting of the SiN membrane chips with holder versions based on clamping the chip down. By now, gluing has been tried out as well in our group, but this shall not be discussed in this thesis.

Two prototype holders were produced, which both basically were compatible with clamping and glueing. The round holder and the square holder. The difference between them was the contact area of membrane and holder. The **round holder** (see fig. 5.2) minimized it as due to the round hole only three corners (the contact area was not perfectly plane) of the membrane touched the holder. The **square holder** (see fig. 5.3), where all four edges of the membrane touched the frame of the square-shaped hole in the holder, was assumed to result in lower Q-factors, because intuitively contact affects the membrane in its movement and therefore decreases Q. This turned out to be wrong, which was favorable for optomechanics experiments in cryogenic environments, as a holder with larger contact area guarantees quicker and better thermalization of the membrane for low temperature measurements.

So we chose the square-type holder for further investigations on the optimal clamping. We tried out fixing all four edges of the chip with one square copper frame, fixing all four edges with a square teflon frame, clamping the chip with two small pieces of teflon at two edges, and clamping the chip with two small pieces of teflon at two corners. The results thereof are presented in the following section.

The ultimate "cavity compatible" holder, that was produced at the end of my measurements, comprised all the knowledge gathered during the previous trials. Besides from having the right size for the cavity, it had a square-shaped hole and the membrane was clamped by two pieces of teflon at two corners.

Another issue was the further investigation of the size of the contact area between holder and membrane. The fact that obviously the least contact area was not automatically correlated with the highest Q-factors, opened a new parameter to be varied, the size of the contact area. The width of the contact rim of both the square-type and the round-type holder needed to be optimized in terms of the balance between high Q and good thermalization.

5.3 Results

Here, the results of the Q-measurements of the different membranes with the holders and clampings described before, at room and low temperature shall be presented.

5.3.1 Several SiN membranes under equivalent conditions

As a start, we measured several SiN Norcada membranes under the same conditions in order to know the deviation of the Q-factors between the single membranes. Moreover, these measurements, which were performed using the round holder without clamping, should serve as a reference for each membrane, to check in later measurements, how much the Q was changed due to the clamping.

The results are illustrated in fig. 5.4. The measurements took place at room temperature and the membranes lay in the round holder without any kind of clamping. Six membranes (membranes 1-4, 6, 10) had dimensions of $0.5 \times 0.5\text{mm} \times 50\text{nm}$ and three (membranes 7-9) of $0.5 \times 0.5\text{mm} \times 100\text{nm}$.

Looking at fig. 5.4, the most striking fact is the **big variation** of the Q-factors of the single membranes. The possibility of destructed membranes is ruled out, since before each measurement, we checked the membrane with an optical microscope. As destruction of the membranes happened quite easily when unpacking them, this was not only a pro forma step, but some devices actually had to be sorted out. Despite the selection, the variation in Q is fairly big between the different membranes, which seems to be a result of the fabrication process. One can see that in particular

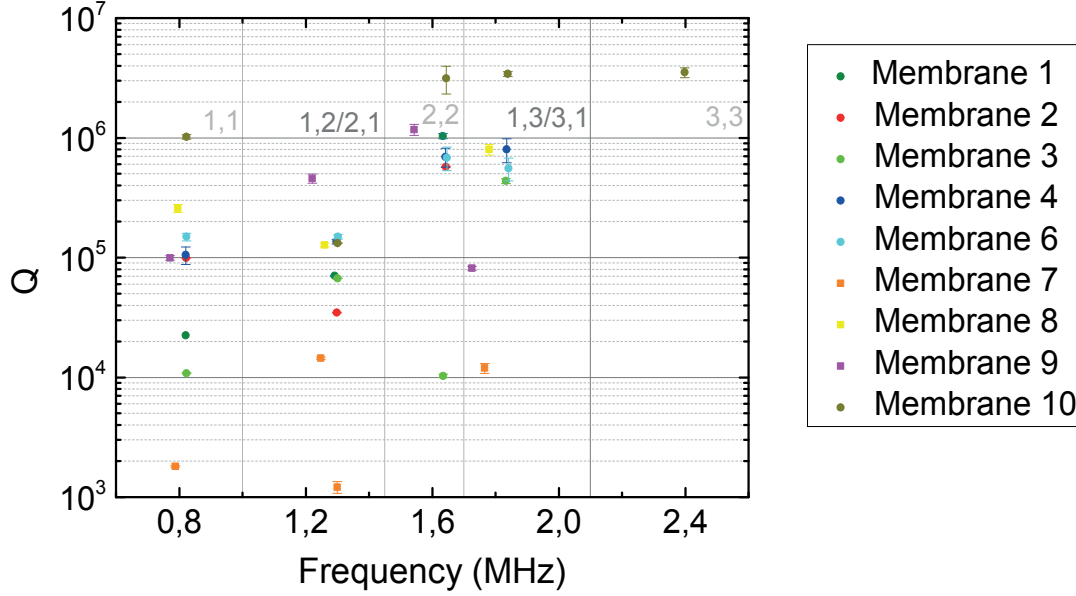


FIGURE 5.4: **Measured Q factors of nine SiN Norcada membranes under identical conditions.** The measurements were performed @ room temperature with the membranes unclamped in the round holder. Membranes of two different dimensions were used: 1-6 and 10: $0.5 \times 0.5\text{mm} \times 50\text{nm}$; 7-9: $0.5 \times 0.5\text{mm} \times 100\text{nm}$.

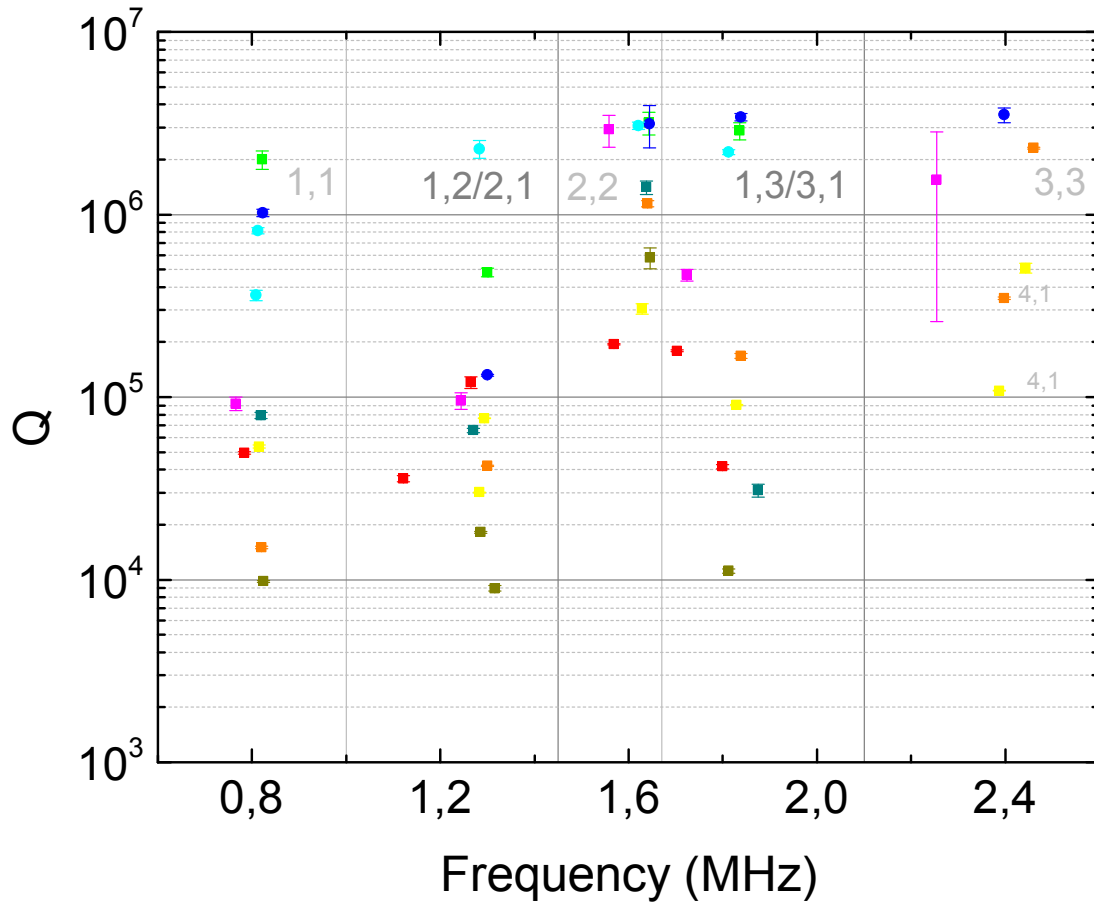
membrane 7 and membrane 3 had generally lower Q-factors than the majority of the other membranes, whereas on the other hand, membrane 10 offers outstanding Q-values.

Apart from the variation between the different membranes, a tendency of differing Q-factors for different **modes** can be noticed. The fundamental mode (denoted by 1,1), which is located at a frequency of around 820kHz, exhibits moderate Q-factors of mostly 10^5 , whereas the 2,2 and 1,3/3,1 (and 3,3) mode often show Q-factors near or beyond 10^6 . Furthermore, the Q-factor of the 2,2 mode varies less between the different membranes than the Q-factor of the other measured modes.

This shows that for cavity optomechanical experiments, a high-Q membrane has to be preselected in addition to mounting it properly.

5.3.2 SiN membrane 10, comparison of all measurements

Next, the dependence of Q on the method of mounting the membrane shall be discussed. First, the influence of the size of the contact area (round/square holder) is determined. Then, the effect of different kinds of clamping is investigated. Experimental tests on the ideal method of mounting the membrane, mainly by gluing the membrane on the holder or putting it on the holder without additional fixation,



- Round holder, unclamped @RT
- Round holder, unclamped @LT
- Square holder, unclamped @RT
- Square holder, Cu frame @RT
- Square holder, teflon frame @RT
- Square holder, teflon on two sides @RT
- Square holder, teflon on two corners @RT
- Cavity compatible holder, teflon on two corners @RT
- Cavity compatible holder, teflon on two corners @LT

FIGURE 5.5: **Comparison of all measurements of membrane 10.** The impact of the holders and the clamping methods can be compared directly.

can also be found in ref. [31], [32].

In order to optimally illustrate the effect of the different holders and clamps, fig. 5.5 depicts all measurements done with membrane 10.

The first conclusion is that the Q-factors basically do not change between the **round** and the **square holder**, as can be deduced from the measurements with the membrane lying unclamped in these two holders, see fig. 5.5. This means that it does not matter dramatically whether the membrane touches the holder only with three corners or on four edges. As mentioned before, this is very convenient, because for thermalization more contact is favorable. Hence, the next holders were designed after this prototype with a square hole and square four-side contact area. The optimal width of the contact rim where the membrane touches the holder has still to be found out experimentally by varying the width and observing the effect on the quality factor.

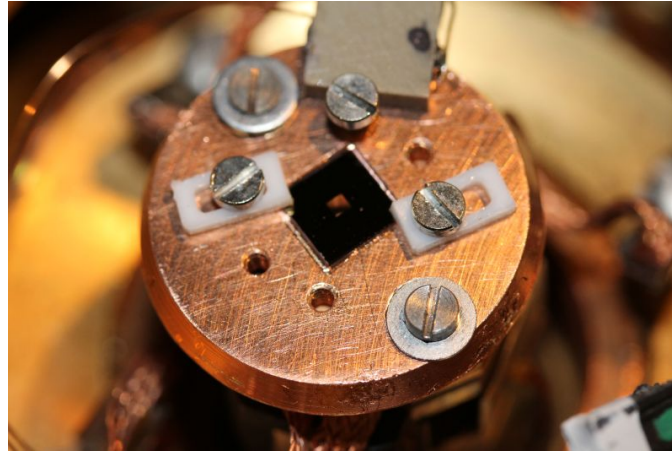


FIGURE 5.6: A SiN membrane in a cavity compatible square holder clamped with teflon on two corners.

Apart from the shape of the holder, the method of **clamping** the SiN chip on the holder was varied. Mechanical clamping means direct contact with the SiN membrane layer, and therefore can decrease the Q-factors significantly. To be more precise, the measurements show that a whole frame, be it made of copper or teflon, completely ruins the Q-factors of all modes. Furthermore, clamping with teflon on two sides or corners (see fig. 5.6) basically results in lower Q-factors as well, but not for the 2,2 and 3,3 modes. They still mostly exhibit Q-factors higher than 10^6 . Therefore, for further experiments requiring high Q-factors, it seems to be sensible to choose the 2,2 or 3,3 mode of a membrane. This is in good accordance with the results from the low temperature measurements.

It is worth noting, that the **resonance frequencies are shifted** to lower frequencies by the clamping. While the frequency difference between the round and the square holder for an unclamped membrane is in average only $1kHz$, in particular the Cu frame has an enormous influence on the resonance frequencies. It causes a deviation of $36kHz$ to $178kHz$ for the different modes compared to the unclamped membrane. The other clamping methods result in a much more modest shift of $11kHz$ in average.

In addition, the clamping, especially the one with the frames, entails a strong **splitting** of the 1,2/2,1 and 1,3/3,1 modes. The copper frame gives rise to a frequency difference of $137.5kHz$ between the 1,2 and the 2,1 modes and $97.08kHz$ between the 1,3 and the 3,1 modes. The teflon frame induces a frequency difference of $29.69kHz$ between the 1,2 and the 2,1 modes. These values are very high compared to a splitting of less than $5kHz$ for unclamped and the other clamped membranes. This means that measuring the splitting can be used to find out how tightly the membrane is clamped onto the holder, which also affects the Q-factors, as we know.

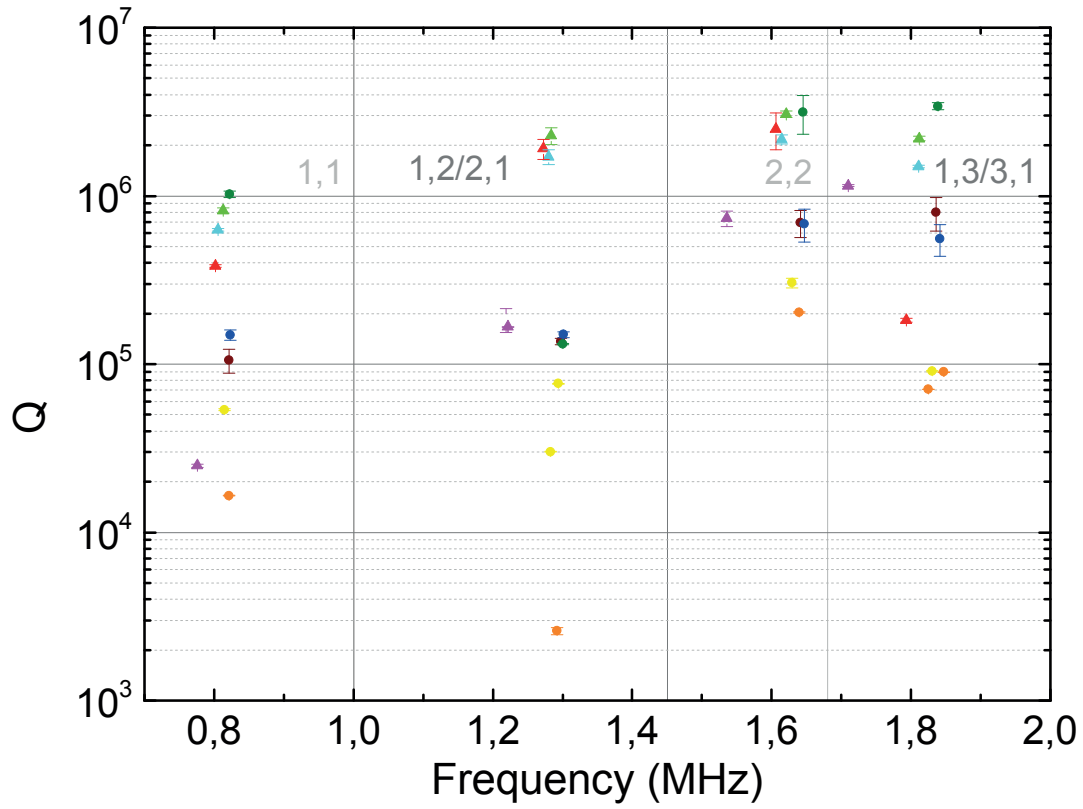
The fact that the splitting for the membranes which were not clamped with a frame was so narrow, was also the reason why we did not measure the Q of the 1,2/2,1 and 1,3/3,1 separately in the majority of the measurements. This separation was not resolved in the ringdown measurements, for which we used a bandwidth of $10kHz$. So both modes were contained in one ringdown. Moreover, the Q-factors of the splitted modes turned out to be of the same order of magnitude.

As an experimental side remark, we want to shortly mention an observation. The influence of the clamping on the Q-factor, on the frequency and on the mode splitting depended to a non-negligible extent on the **tightness** of the clamping. Tight clamping entailed significant effects, whereas very loose clamping reproduced more or less the results from the measurements without clamping.

5.3.3 Comparison of Q of SiN membranes at room and low temperature

A potential means to generally enhance the mechanical quality factor Q - independent of holder and clamping - is cooling the membranes to cryogenic temperatures. Therefore, the next step was to cool the membranes in the cryostat with Helium 4, and observe the effect on the Q-values. Tests on the temperature dependence of the quality factor of stoichiometric SiN membranes were also performed in ref. [29], [30].

The data in fig. 5.7 confirms the initial assumption of improved Q. In average, the **Q-factors** of the membranes are higher by a factor of 4.5. Two remarks are to be made on that number. First, there are membranes, or at least single modes of some membranes, for which the opposite is true, namely lower Q at low tempera-



- Membrane 4, round holder, no clamping @RT
- ▲ Membrane 4, round holder, no clamping @LT
- Membrane 6, round holder, no clamping @RT
- ▲ Membrane 6, round holder, no clamping @LT
- Membrane 10, round holder, no clamping @RT
- ▲ Membrane 10, round holder, no clamping @LT
- Membrane 4, cavity compatible holder, teflon on 2 corners @RT
- ▲ Membrane 4, cavity compatible holder, teflon on 2 corners @LT
- Membrane 10, cavity compatible holder, teflon on 2 corners @RT
- ▲ Membrane 10, cavity compatible holder, teflon on 2 corners @LT

FIGURE 5.7: **Comparison of measured Q factors @ room temperature and low temperature.** On average, the Q factors are higher at cryogenic temperatures by a factor of 4.5.

tures. Second, there are certain modes, which benefit more from low temperatures than others, like the 1,2/2,1 mode.

The increase of the quality factor at cryogenic temperatures is in good accordance with other experimental results, e.g. in ref. [29], [30]. For further applications, which require high Q-factors, the most reasonable mode to take is the 2,2 mode. This is in accordance with the previous measurements. I cannot make a statement about the 3,3 mode at low temperatures as its peak was not visible on the spectrum analyzer for unknown reasons, and it therefore could not be measured.

The measurement of the 3,3 mode also caused problems at room temperature. The general difficulty with the higher order modes might occur because the correct positioning of the laser spot on the membrane, resulting in good coupling of the beam to the mode, becomes more difficult with increasing mode number and therefore decreasing mode size. At cryogenic temperatures it was even more difficult to find the 3,3 peak. This might originate from the fact that the noise power spectrum is proportional to the temperature, which means that the resonance peak at cryogenic temperatures exceeds the electronic noise floor less than at room temperature. In addition, the resonance frequencies experienced a continuous shift to lower frequencies during the cooling sessions, as will be described in the next paragraph, which made it sometimes difficult to find and measure the ringdown of a certain mode.

Apart from the enhancement of Q, another phenomenon could be observed at low temperatures, namely the **shift of the resonance frequencies to lower frequencies**, as mentioned before. This might result from the different thermal expansion coefficients α for Si and SiN. The Si frame with $\alpha_{Si} \approx 3 \times 10^{-6} K^{-1}$ shrinks more than the SiN membrane with $\alpha_{SiN} \approx 2 \times 10^{-6} K^{-1}$, such that the membrane in the frame is less stressed, i.e. the tensile stress σ decreases, and therefore the frequency decreases as well according to $f_{m,n} = \sqrt{\frac{\sigma}{4\rho}[(\frac{m}{l})^2 + (\frac{n}{w})^2]}$, where ρ is the density of the material, m, n is the mode number and l, w are the side lengths of the membrane. Fig. 5.8 shows percentage resonance frequency shifts after approximately three hours of cooling. The measurements were done on three membranes in the round holder without clamping and on one membrane in the cavity compatible holder (which is a square-type holder) with clamping.

There is no distinction between the modes as the observed relative frequency shift due to cooling is roughly the same for all modes. In the case of the unclamped membrane in the round holder, it ranges from 1.1 to 2.3%. For the clamped membrane in the square-type cavity compatible holder, the shift is again similar for all modes, but it is generally higher, from 3 to 7.7%. This could be explained by the faster thermalization in this holder with larger contact area. Once we have a means to measure the actual temperature at the membrane, we could make a calibration relating the observed frequency shift to the temperature at the membrane, such that we could know if the membrane is at the lowest temperature by looking at the frequency shift.

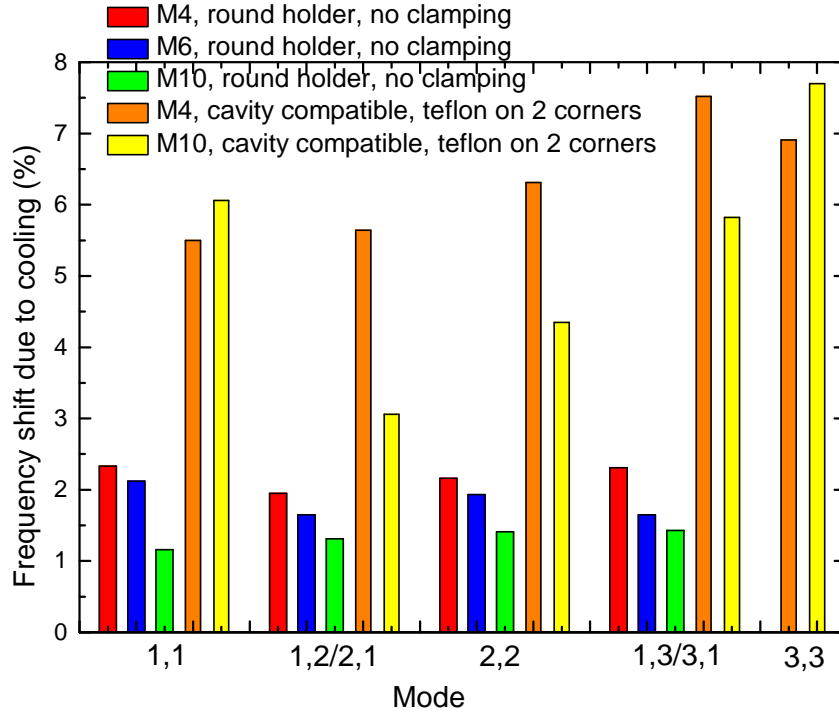


FIGURE 5.8: **Comparison of mode frequencies between room temperature and low temperature.** The percentage frequency shift due to cooling is approximately equal for all modes. The overall stronger frequency shift of the membranes in the cavity compatible holder can probably be ascribed to the faster thermalization (all the measurements were done at roughly the same time after the cool-down start) of membranes in this holder, which - similarly to the square holder - possesses a square-shaped contact area. The frequencies continued shifting downwards until the end of all cool-down sessions. That means that we have never reached the state of final thermalization of the membrane.

The process of the **thermalization** of the membrane seemed to take a very long time with both holders. We have probably done all our measurements with not yet completely thermalized membranes. The reason for this assumption is the fact that the frequency drift did never stop until the end of the low temperature measurement session. The permanent frequency drift during the measurement occurred although we started measuring only when the temperature sensor at the sample holder displayed a constant temperature (around 30K). But this solely guaranteed for the thermalization of the holder, not of the membrane itself. There was no option to directly measure the membrane temperature.

In spite of those difficulties, the membranes must have been significantly cooled, since an improvement of the Q-factors was clearly visible. So it is justified to speak of low temperature measurements.

5.4 Summary

The above results show that the silicon nitride Norcada membranes themselves exhibit a large variation in their Q-factors due to their fabrication. Cooling to cryogenic temperatures on average enhances Q by a factor of 4.5. Clamping of the membrane decreases Q, the best solution among the tested ones were pieces of teflon at two corners.

All the measurements make clear that the 2,2 or 3,3 mode exhibit the highest quality factors.

Furthermore, minimal contact area between membrane and holder does not give the best results. This is an advantage for cooling the membranes as faster thermalization is possible with larger contact area.

So the next tasks for further improvements of Q would be the investigation of the ideal size of the contact area between membrane and holder, other methods of clamping, other holder or clamp materials, and gluing.

Already now, with the tested holders and clamping methods, Q-factors beyond 10^6 are quite achievable and reproducible, which is a satisfactory result that can be employed in optomechanical experiments.

6 Conclusion and Outlook

In order to enable cavity optomechanics, the system of mechanics and light must be well isolated from the environment, while showing a good coupling between the mechanical device and the light. For this purpose, the mechanical element in the cavity plays a crucial role. It must exhibit good mechanical properties, expressed by the mechanical Q-factor, to lower dissipation of energy into the environment. If the device is used as a cavity end-mirror, good optical properties, expressed by the Finesse, or the reflectivity in a first step, are required as well.

In this thesis, three optomechanical devices are investigated.

First, we designed mechanical devices that have an additional silicon pillar between the mirror pad and the mechanical resonator, which should lead to less influence of the mirror material on the mechanics, and therefore result in enhanced mechanical Q-factors. These structures still have to be fabricated and tested.

Further, self-built SiN photonic crystal membranes are explored in a setup where a laser beam hits them perpendicularly, without using a cavity. The wavelength and the value of their maximal reflectivity is measured. Theoretical simulations are confirmed in both, the wavelength and the value of the peak reflectivity. This means that good control over the parameters has already been achieved and devices that have to fulfil special requirements can be fabricated in a reproducible way. The values of the maximal reflectivities approach 1 according to the measurements, which means that photonic crystal membranes fulfil the optical requirements for being used as cavity end mirrors. To get more accurate values of reflectivity and Finesse, an optical cavity should be built with the membranes. Not only the photonic crystal membranes' excellent optical properties could be shown, but also good mechanical properties. With the combination of high reflectivity and Q-factors around 10^6 , they have the potential to become an important alternative device in cavity optomechanics.

Finally, the mechanical properties of commercial stoichiometric SiN membranes have been tested. Q-factors exceeding 10^6 were found.

The membranes were clamped to different holders in various ways, and measured at room temperature and at cryogenic temperatures. As expected, clamping with less contact improves the Q-factors, as well as low temperatures enhance it by almost a factor of 5. Concerning the shape of the holders, especially the contact area between holder and membrane, there still has to be found a balance between little contact resulting in higher Q and more contact resulting in better thermalization of

6 *Conclusion and Outlook*

the membrane when cooling it. Apart from that, the Q-factors of different modes exhibit high variations for the modes we measured (fundamental 1,1 to 3,3). 2,2 and 3,3 are the modes with the best quality factors.

Bibliography

- [1] E. Verhagen, S. Deléglise, S. Weis, A. Schliesser, and T. J. Kippenberg. Quantum-coherent coupling of a mechanical oscillator to an optical cavity mode. *Nature*, 482, 63, 2012.
- [2] K. Stannigel, P. Rabl, A. S. Sørensen, P. Zoller, and M. D. Lukin. Optomechanical transducers for long-distance quantum communication. *Physical Review Letters* 105, 220501, 2010
- [3] R. Riedinger. Optomechanical state reconstruction and optical noise reduction for cavity optomechanics experiments, Master thesis. *Philipps Universität Marburg*, 2013.
- [4] S. Camerer, M. Korppi, A. Jöckel, D. Hunger, T. W. Hänsch, and P. Treutlein. Realization of an Optomechanical Interface Between Ultracold Atoms and a Membrane. *Physical Review Letters* 107, 223001, 2011.
- [5] M. Aspelmeyer, P. Meystre, and K. Schwab. Quantum optomechanics. *Physics today*, July 2012, page 29-33.
- [6] P. Zoller and C. W. Gardiner. Quantum Noise. *Springer Berlin / Heidelberg / New York*, 3 edition, 2004.
- [7] M. Aspelmeyer, T. J. Kippenberg, F. Marquardt. Cavity Optomechanics. *arXiv:1303.0733v1*, 2013.
- [8] G. D. Cole, I. Wilson-Rae, K. Werbach, M. R. Vanner, and M. Aspelmeyer. Phonon-tunnelling dissipation in mechanical resonators. *Nature Communications* 2:231-238, 2011.
- [9] R. Lifshitz and M.L. Roukes. Thermoelastic damping in micro- and nanomechanical systems. *Physical Review B*, Volume 61, 5600, 2000.
- [10] B. Zwickl. Progress toward observation of radiation pressure shot noise, Ph.D. thesis. Yale, 2011.
- [11] C. Zener. Internal friction in solids, I. Theory of internal friction in reeds. *Physical Review* 52, 230–235, 1937.
- [12] C. Zener. Internal friction in solids, II. General theory of thermoelastic internal friction. *Physical Review* 53, 90-99, 1938.

- [13] A. A. Kiselev, G. J. Iafrate. Phonon dynamics and phonon assisted losses in Euler-Bernoulli nanobeams. *Physical Review B* 77, 205436, 2008.
- [14] J. F. Vignola, J. A. Judge, J. Jarzynski, M. Zalalutdinov, B. H. Houston et al. Effect of viscous loss on mechanical resonators designed for mass detection. *Applied Physics Letters* 88, 041921, 2006.
- [15] D. J. Keating, Dr. L. Ho. Effects of squeezed film damping on dynamic finite element analyses of MEMS. *IntelliSense Corporation*.
- [16] M. Bao, H. Yang, H. Yin, and Y. Sun. *Journal of Micromechanics and Microengineering* 12, 341, 2002.
- [17] Q. P. Unterreithmeier, T. Faust, J. P. Kotthaus. Damping of nanomechanical resonators. *Physical Review Letters* 105, 027205, 2010.
- [18] P. Mohanty, D. A. Harrington, K. L. Ekinici, Y. T. Yang, M. J. Murphy, and M. L. Roukes. Intrinsic dissipation in high-frequency micromechanical resonators. *Physical Review B* 66, 085416, 2002.
- [19] C. Seoáñez, F. Guinea, A. H. Castro Neto. Surface dissipation in nano-electromechanical systems: unified description with the standard tunneling model and effects of metallic electrodes. *Physical Review B* 77, 125107, 2008.
- [20] T. Faust, J. Rieger, M. J. Seitner, J. P. Kotthaus, and E. M. Weig. Signatures of two-level defects in the temperature-dependent damping of nanomechanical silicon nitride resonators. *arXiv:1310.3671*, 2013.
- [21] G. Anetsberger, R. Riviere, A. Schliesser, O. Arcizet, and T. J. Kippenberg. Ultralow-dissipation optomechanical resonators on a chip. *Nature Photonics* 2, 627–633, 2008.
- [22] J. Clark, W.-T. Hsu, M. Abdelmoneum, and C.-C. Nguyen. High-Q UHF micromechanical radial-contour mode disk resonators. *Journal of Microelectromechanical Systems* 14, 1298–1310, 2005.
- [23] K. Wang, A.-C. Wong, and C.-C. Nguyen. VHF free-free beam high-Q micromechanical resonators. *Journal of Microelectromechanical Systems* 9, 347–360, 2000.
- [24] I. Wilson-Rae. Intrinsic dissipation in nanomechanical resonators due to phonon tunneling. *Physical Review B* 77, 245418, 2008.
- [25] S. Chakram, Y.S. Patil, L. Chang, M. Vengalattore. Dissipation in ultrahigh quality factor SiN resonator membranes. *arXiv:1311.1234v1*, 2013.

- [26] S. J. Orfanidis. Electromagnetic waves and antennas. *Rutgers University*, 2002.
- [27] D. Joannopoulos, S. G. Johnson, J. N. Winn, and R. D. Meade. Photonic Crystals. *Princeton University Press*, 2008.
- [28] J. Hofer. A scanning optical fiber interferometer for the characterization of microscale mechanical oscillators, Bachelor thesis. *Universität Wien*, 2011.
- [29] D. R. Southworth, R. A. Barton, S. S. Verbridge, B. Ilic, A. D. Fefferman, H. G. Craighead, and J. M. Parpia. Stress and Silicon Nitride: A Crack in the Universal Dissipation of Glasses. *Physical Review Letters* 102, 225503, 2009.
- [30] B. M. Zwickl, W. E. Shanks, A. M. Jayich, C. Yang, A. C. Bleszynski Jayich, J. D. Thompson, and J. G. E. Harris. High quality mechanical and optical properties of commercial silicon nitride membranes. *Applied Physics Letters* 92, 103125, 2008.
- [31] D. J. Wilson, C. A. Regal, S. B. Papp, and H. J. Kimble. Cavity optomechanics with stoichiometric SiN films. *Physical Review Letters* 103, 207204, 2009.
- [32] D. J. Wilson. Cavity optomechanics with high-stress silicon nitride films, PhD thesis. *California Institute of Technology*, 2012.
- [33] S. Gröblacher. Quantum opto-mechanics with micromirrors: combining nano-mechanics with quantum optics, PhD thesis. *Universität Wien*, 2010.
- [34] T. P. Purdy, R. W. Peterson, P.-L. Yu, and C. A. Regal. Cavity optomechanics with Si₃N₄ membranes at cryogenic temperatures. *arXiv:1208.6560v1*, 2012.
- [35] T. P. Purdy, R. W. Peterson, and C. A. Regal. Observation of Radiation Pressure Shot Noise on a Macroscopic Object. *arXiv:1209.6334v2*, 2013.
- [36] M. Aspelmeyer, S. Gröblacher, K. Hammerer, and N. Kiesel. Quantum optomechanics—throwing a glance. *Journal of the Optical Society of America B* 27, 6, 2010.
- [37] P. Meystre. A short walk through quantum optomechanics. *arXiv:1210.3619v1*, 2012.
- [38] F. Marquardt, S. M. Girvin. Optomechanics. *Physics* 2, 40, 2009.
- [39] W. Zurek, S. Habib, and J. Paz. Coherent states via decoherence. *Physical Review Letters*, 70(9):1187-1190, 1993.

- [40] P. Pearle. Reduction of the state vector by a nonlinear Schroedinger equation. *Physical Review D*, 13(4):857-868, 1976.
- [41] R. Penrose. Wavefunction collapse as a real gravitational effect. *Mathematical physics*, pages 266-282, 2000.
- [42] T. Ramos, V. Sudhir, K. Stannigel, P. Zoller, T. J. Kippenberg. Nonlinear Quantum Optomechanics via Individual Intrinsic Two-Level Defects. *arXiv:1302.1855v2*, 2013.
- [43] S. Gröblacher, J. B. Hertzberg, M. R. Vanner, G. D. Cole, S. Gigan, K. C. Schwab, and M. Aspelmeyer. Demonstration of an ultracold micro-optomechanical oscillator in a cryogenic cavity. *Nature Physics*, 5(7):485-488, 2009.
- [44] N. Kiesel, F. Blaser, U. Delic, D. Grass, R. Kaltenbaek, M. Aspelmeyer. Cavity cooling of an optically levitated nanoparticle. *PNAS*, 11, 35, 14180-14185, 2013.
- [45] T. O. Woodruff and H. Ehrenreich. Absorption of sound in insulators. *Physical Review* 123, 1553, 1961.
- [46] H. E. Bömmel and K. Dransfeld. Excitation and attenuation of hypersonic waves in quartz. *Physical Review* 117, 1245, 1960.
- [47] E. G. Williams. A series expansion of the acoustic power radiated from planar sources. *Journal of the Acoustical Society of America* 73, 1520, 1983.

Curriculum Vitae

Karoline Siquans



Education

2000-2008	BG/BRG Franklinstraße 21, Vienna, Austria
2008-2011	University of Vienna, Faculty of Physics, Bachelor degree program
2011-2014	University of Vienna, Faculty of Physics, Master degree program

Employment

2009-2011	Tutor for “Physikalisches Praktikum für BiologInnen”, University of Vienna
2013	Research assistant in the group of Markus Aspelmeyer, University of Vienna

Scholarships

2011/12	Leistungsstipendium, University of Vienna
---------	-------------------------------------------